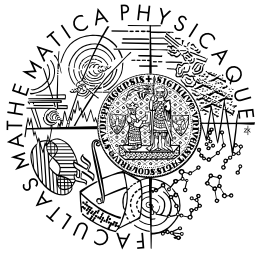

FACULTY
OF MATHEMATICS
AND PHYSICS
Charles University

Summary of doctoral thesis

Libor Šachl

Modelling of global ocean circulation and ocean-induced magnetic field

Department of geophysics

Supervisor of the doctoral thesis: Prof. RNDr. Zdeněk Martinec, DrSc.
Study programme: Physics
Study branch: Geophysics

Prague 2020

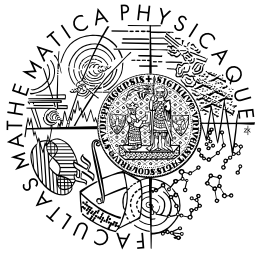

MATEMATICKO-FYZIKÁLNÍ FAKULTA
Univerzita Karlova

Autoreferát dizertační práce

Libor Šachl

Modelování globální oceánské cirkulace a oceánem indukovaného magnetického pole

Katedra geofyziky

Vedoucí disertační práce: Prof. RNDr. Zdeněk Martinec, DrSc.
Studijní program: Fyzika
Studijní obor: Geofyzika

Praha 2020

Dizertace byla vypracována na základě výsledků získaných v letech 2011–2020 během doktorandského studia na Katedře geofyziky MFF UK a Dublin Institute for Advanced Studies.

Dizertant:
Mgr. Libor Šachl
Katedra geofyziky MFF UK
V Holešovičkách 2, 180 00, Praha 8

Školitel:
Prof. RNDr. Zdeněk Martinec, DrSc.
Katedra geofyziky MFF UK
V Holešovičkách 2, 180 00, Praha 8
Dublin Institute for Advanced Studies
5 Merrion Square, Dublin 2, Ireland

Oponenti:
Jun.-Prof. Dr. Michael Schindelegger
University of Bonn, Institut of Geodesy and Geoinformation (IGG)
Nussallee 15, 53115, Bonn, Germany

Prof. Hiroaki Toh
Graduate School of Science, Kyoto University
Sakyo, 606-8502, Kyoto, Japan

Předsedkyně oborové rady:
Doc. RNDr. Hana Čížková, Ph.D.
Katedra geofyziky MFF UK
V Holešovičkách 2, 180 00, Praha 8

Obhajoba dizertace se koná dne 23. 9. 2020 od 10.00 hodin před komisí pro obhajoby dizertačních prací v oboru Geofyzika v budově MFF UK, Ke Karlovu 3, Praha 2 v místnosti M252.

S dizertací je možno se seznámit v PGS MFF UK, Ke Karlovu 3, Praha 2.

Contents

Introduction

The ocean modelling community commonly use several renown ocean general circulation models (OGCMs) such as NEMO, MOM and FESOM. These models have been developed by research groups for many years, which resulted in complex mathematical and numerical algorithms. There are geophysically relevant problems, such as the glacial isostatic adjustment, in which the global ocean plays an important role. Ocean circulation does not need to be modeled extremely complex, but other phenomena such as time changing geometry of ocean domain needs to be considered. Geophysical applications motivated us to develop a new OGCM called LSOMG. The LSOMG model is not meant to substitute the existing OGCMs but to provide a modelling framework for geophysical rather than purely oceanographic applications. LSOMG is a 3-D baroclinic ocean model fully parallelized using the MPI standard. It is forced by atmospheric fluxes (wind stresses, heat fluxes, etc.) but also by tides. The model can be run in a simplified 2-D barotropic version if 3-D effects can be neglected. LSOMG was tested in a series of simplified barotropic numerical tests: the tsunami and tidal numerical

tests and the Munk problem. In the full baroclinic version, we tested the generation of the Ekman layer and the advection of tracers. Finally, we present realistic wind and tidally driven ocean circulations computed by the LSOMG model.

The second part of the thesis is devoted to the study of ocean-induced magnetic field (OIMF). The ultimate goal is to extract information about the ocean circulation from the observed OIMF, e.g., by Swarm satellites, and assimilate it into an OGCM. However, it is a challenging task since the OIMF has small amplitudes of about 2 nT maximum at Swarm altitudes. It is overlaid by the main, ionospheric and magnetospheric magnetic fields that are several orders of magnitude larger. We thus focus on the precision of forward modelling and study the impact of physical and numerical approximations. Namely, we inspected the impact of galvanic coupling, vertical stratification of ocean flow and electrical conductivity, self-induction and horizontal resolution on the numerically predicted OIMF. Another possibility is to use localized magnetic measurements at the sea bottom instead of satellite data. Consequently, we studied the toroidal magnetic field inside the ocean using fully 3-D versions of both LSOMG and the magnetic-induction solver ElmgTD. The toroidal magnetic field is zero at the surface but it is significant inside the ocean. According to our computations, its magnitude can reach 15 nT, i.e., it is about one order of magnitude larger than the OIMF at satellite altitudes.

1 Ocean model LSOMG

1.1 Motivations and requirements

Our motivation for the development of the LSOMG model was the intention to have an OGCM that is

- a global primitive-equation ocean model
- fully 3-D not only barotropic and thus it is capable of generating the 3-D distribution of 3-D velocities (important, for example, for the modelling of toroidal magnetic field in the ocean)
- open for modifications
- understood on a code level by our group
- usable for geophysical purposes, such as modelling the ocean induced magnetic field

We have chosen the LSG ocean model which was developed at the Max–Planck–Institut für Meteorologie in Germany. The main reason for our choice was the model designation for large-scale long-term simulations, for example, climate studies. Such model is certainly not suitable for regional studies of eddy activity but its complexity could be sufficient for the geophysical applications. On top of that, a simplified numerical core implies faster computations and a light-weight tool for the user/programmer.

The model fulfils our first and second requirements. The third requirement is also fulfilled. We obtained the LSG code from Dr. Butzin and we were free to

modify it. The fourth requirement is fulfilled only partly. The model is described in Maier-Reimer and Mikolajewicz [1992]. The text is meant to be the LSG manual but it is incomplete. The code is not commented frequently either, which makes its understanding difficult. The fifth requirement is invalid. It turned out during the development that the LSG model is obsolete. We have gradually rewritten the whole code with the exception of several parts, such as the advection scheme QUICK or the sea-ice model. The major modifications are summarized in Sec. 1.2 and in Table 1. As a consequence, we call the resulting model LSOMG since the original acronym LSG is now inaccurate and misleading. The LSOMG is the shortcut for the "Libor Sachl Ocean Model for Geophysics".

Note that the LSOMG model is fully 3-D but it can also be run in a barotropic version. We call this version LSOMG-BT. It can be used to test the barotropic part of the LSOMG model, see Sec. 1.5, or to model the tidal circulation, see Sec. 1.6.

1.2 Summary of differences between the LSG and LSOMG models

Both the LSG and LSOMG models discretize the governing equations using the finite difference method. The LSG model uses the Arakawa E-grid while the LSOMG model is build on the Arakawa C-grid. The main motivation to switch from the E-grid to C-grid was to avoid the coexistence of two solutions that evolve independently of each other on the E-grid . A more natural treatment of boundary conditions and simpler indexing of grid points are additional advantages. Barotropic LSOMG-BT supports also Arakawa grids B and E for certain time stepping schemes as an alternative to the default C-grid.

The governing equations in the LSG model are expressed in the spherical coordinates. It is a valid option but it is not free of deficiencies, as discussed in Sec. 2.2 of the thesis. In the LSOMG model, we rather implemented the governing equations in their general form using the metric coefficients of the particular coordinate system. Consequently, the LSOMG model is able to handle arbitrary orthogonal horizontal coordinates. The suitable coordinate grids are listed in Sec. 2.2 of the thesis. There are three generalized grids available in the LSOMG model: the dipolar grid of Roberts et al. [2006], the tripolar confocal grid of Murray [1996] and the tripolar reprojected grid of Murray [1996] which we prefer. Note that apart from the general forms of operators in the model, the programs that regrid data on the computational grids also need special attention. We calculate the model bathymetry by averaging data values within model grid cells which requires an algorithm to determine the position of data point with respect to the particular grid cell. Besides that, vector data such as 10-m wind speed need to be rotated into the direction of coordinate axes of the chosen coordinate system.

The ad-hoc choice of vertical layers in the LSG model has been replaced by a semi-automatically generated distribution of vertical layers in the LSOMG model. The distribution is determined from a prescribed smooth distribution of level depths and thicknesses. The scheme is not fully automatic because it contains one tunable parameter.

The original LSG model propagates the barotropic part of the momentum

equation in time using the implicit time stepping scheme. The implicit scheme allows to step the model forward in time with a significantly larger time step than the explicit scheme. On the other hand, the implicit scheme requires to solve a system of linear equations in each time step. Our primary goal was to model the wind- and buoyancy-driven ocean circulation but we also intended to force the model by tides. The accurate tidal modelling requires the time step to be "small enough" to resolve the tidal periods. The period of principal lunar semidiurnal M_2 tide is approximately 12.4 hours, which means that a tidally-driven model needs to resolve much finer time scales than a purely wind-driven model. The implicit time-stepping scheme with a short time step could become time consuming due to the need to repeatedly solve the system of linear equations. The explicit time-stepping scheme is thus better suited for the tidal modelling. Several time-stepping schemes for the barotropic system are available in the LSOMG model, see Sec. 1.3.

The vertically dependent baroclinic forcing in the original LSG model includes pressure gradient and horizontal friction force while the vertical friction force and nonlinear terms are neglected. Both terms are now available. The nonlinear terms are expressed either in the vector invariant form or in the flux form. The implementation follows Madec [2012]. The vertical friction arises from the vertical shears of horizontal velocities. The term is discretized implicitly in time to ensure stability even for large vertical eddy viscosity.

The horizontal friction force has already been present in the LSG model, however, its implementation has been improved. The LSG models uses the horizontal friction in the form of a Laplacian. The LSOMG model retains this option but a more appropriate form given by Murray and Reason [2001] is also available. Similarly, horizontal viscosities are constant in LSG but LSOMG enables viscosities which adapt according to the actual velocity field [Smagorinsky, 1963, 1993].

The form of diffusion operator has also been improved. There are two options available for the tracer diffusion operator at present. It is either the original Laplacian operator or the epineutral (isopycnal) operator. The Laplacian is a somewhat ad-hoc form, on the contrary, the epineutral operator is based on oceanographic measurements and observations and it is thus physically justified. The implementation of epineutral operator is based on the triad algorithm of Griffies et al. [1998] with modifications introduced by Madec [2012] and it is combined with the parameterization of tracer stirring by mesoscale eddies.

The surface heat fluxes are represented by a simple relaxation towards the prescribed distribution of sea surface temperature in the LSG model. This option is retained in the LSOMG model but it is supplemented with more realistic bulk formulas for shortwave, longwave, sensible and latent heat fluxes. The bulk formulas of Kara et al. [2002], Kondo [1975] and Large and Yeager [2004] are available.

The tidal forcing is expressed in the form of a gradient of the second-degree tidal potential. The implementation is adopted from the DEBOT model. The LSOMG also includes parameterizations of two important physical phenomena:

- The internal wave drag caused by the breaking of internal tidal waves. The parameterization of Jayne and St. Laurent [2001] has been implemented.

- The change of gravity field due to the effect of self attraction and loading

(SAL). The scalar approximation of SAL has been implemented into the LSOMG model.

New tracer advection schemes have been implemented to the LSOMG model. The original QUICK scheme from the LSG model has been supplemented (replaced) with three schemes with flux limiters: The Lax-Wendroff scheme, third-order direct space time scheme [Adcroft et al., 2014] and the scheme of Smith et al. [2010]. The splitting method of Adcroft et al. [2014] has been implemented to handle the multidimensional tracer advection.

The original EOS-80 state equation [UNESCO, 1981] has been replaced by the state equation of [Jackett et al., 2006]. The initial potential temperature distribution is obtained from the in-situ temperature distribution following the method of McDougall et al. [2003].

The convective adjustment scheme used in the LSG model checks the stability of a water column from top to bottom and if instability is found, the scheme mixes the content of two neighbouring grid cells. The procedure is finished when it reaches the bottom cell, it is not repeated. It is a simple and computationally favourable scheme but it does not guarantee to stabilize an unstable water column. The LSOMG model thus employs a scheme of Rahmstorf [1993] which truly guarantees to stabilize an arbitrary unstable water column.

The LSG ocean model is coded in the old fashioned way in FORTRAN 77 with common blocks and static arrays. The LSOMG model is coded in Fortran 90 with modules and allocatable arrays.

The LSG ocean model is not parallelized at all and it does not utilize any numerical library (e.g., a system of linear equations is solved using a hand-made Gaussian elimination without pivotation). The LSOMG model is parallelized using the MPI standard and it benefits from the sophisticated Intel MKL library if certain parts of the model are active.

The Coriolis term is discretized implicitly in the LSG ocean model. It increases the model stability at no additional computational costs. On the contrary, the discretization of the Coriolis term in both space and time is a delicate issue on the Arakawa C-grid. The Coriolis term in the LSOMG model is discretized using the Adams-Bashforth method in time and there are several spatial schemes available. However, none of the discretizations is completely free of the grid-scale noise. In order to remedy this problem, we implemented the divergence damping and the dual-step five-point-involved spatial smoothing method of Han [2014] into the LSOMG model.

For the reader's convenience, we summarize the key differences between the LSG and LSOMG models in Table 1.

1.3 Barotropic LSOMG-BT model

The LSOMG-BT model is the barotropic version of the LSOMG model. The governing equations of the barotropic ocean model are the so-called shallow water equations (SWE), see Einšpigel and Martinec [2015] for their detailed derivation. SWE can be expressed in two equivalent forms, the flux form and advective form [Williamson et al., 1992]. The advective form expressed in the barotropic velocity

	LSG	LSOMG
Horizontal grid	Arakawa E grid	Arakawa C grid
Horizontal coord.	spherical	generalized
Vertical grid	manually generated	semi-auto generated
Time stepping	no splitting, collocated	splitting, staggered
Barotropic part	implicit	explicit (PC, FBgen)
Horiz. friction	"rotated" Laplacian	Laplacian, "full" form
Vert. friction	no	yes (explicit, implicit)
Nonlinear terms	no	yes (2 formulations)
Isopycnal mixing	no	yes
GM stirring	no	yes
State equation	UNESCO [1981]	Jackett et al. [2006]
Tidal forcing	no	yes (from DEBOT)
Heat fluxes	relaxation	relaxation, bulk formulas
Tidal parameterizations	no	yes
Advection scheme	QUICK	QUICK, LW, DST3
Coriolis term	implicit	Adams-Bashforth
Convective adj.	one sweep	[Rahmstorf, 1993]
Programming	FORTRAN 77	Fortran 90
Parallelization	no	MPI, (OpenMP)

Table 1: Summary of major differences between LSG and LSOMG models. See the main text for more details. PC = predictor-corrector, FBgen = generalized forward-backward, LW = Lax-Wendroff, DST3 = third-order direct space time

$\bar{\mathbf{u}}$ is

$$\bar{\mathbf{u}}_{,t} + \bar{\mathbf{u}} \cdot \nabla_h \bar{\mathbf{u}} + f\mathbf{e}_3 \times \bar{\mathbf{u}} + g\nabla_h \eta = \mathbf{F}, \tag{1}$$

$$\eta_{,t} + \nabla_h \cdot (h\bar{\mathbf{u}}) = 0, \tag{2}$$

the flux form expressed in the vertically integrated transport $\mathbf{U} = h\bar{\mathbf{u}}$ is

$$\mathbf{U}_{,t} + \nabla_h \cdot \left(\frac{\mathbf{U} \otimes \mathbf{U}}{h}\right) + f\mathbf{e}_3 \times \mathbf{U} + gh\nabla_h \eta = h\mathbf{F}, \tag{3}$$

$$\eta_{,t} + \nabla_h \cdot \mathbf{U} = 0, \tag{4}$$

where $f = 2\Omega \sin\phi$ is the Coriolis parameter, where Ω is the angular velocity of the Earth's rotation and ϕ is the latitude, $\mathbf{e}_3$ is the unit vector parallel to the local vertical direction, g is the gravitational acceleration, η is the sea surface height (SSH), h is the water-column height, $\mathbf{F}$ is the forcing, $a_{,t}$ denotes partial derivatives of a with respect to time and ∇_h is the two-dimensional (2-D) horizontal gradient operator. In the LSOMG-BT model, $\mathbf{F}$ contains the horizontal friction $\mathbf{F}_H^{(\mathbf{u})}$, bottom friction $\boldsymbol{\tau}_b$, wind stress $\boldsymbol{\tau}_w$ and tidal forcing $\mathbf{F}_{tid}$,

$$\mathbf{F} = \mathbf{F}_H^{(\mathbf{u})} - \frac{\boldsymbol{\tau}_b}{h} + \frac{\boldsymbol{\tau}_w}{\rho_0 h} + \mathbf{F}_{tid}, \tag{5}$$

where ρ_0 is the constant reference density.

The LSOMG-BT model neglects nonlinear advection in the momentum equation which is represented by the second term on the left-hand side of Eqs. (1)

and (3). As already mentioned in Sec. 1.1, the expected usage of LSOMG-BT is either testing of the barotropic part of the full LSOMG model or modelling of barotropic tidal circulation. Considering the first case, the nonlinear advection terms are computed in the baroclinic part of the model and then inserted into the barotropic part as the vertically integrated baroclinic contribution. Considering the second case, the linear SWE are commonly used in the barotropic tidal models. The nonlinearities become important in shallow coastal regions but on the deep ocean they can be neglected.

The governing equations are discretized using the finite difference method in the LSOMG-BT model. Spatial derivatives are approximated using the centered differences on Arakawa grids [Arakawa and Lamb, 1977]. We consider either free-slip or no-slip boundary conditions. The LSOMG-BT model supports Arakawa grids B, C and E. We apply free-slip boundary conditions on the Arakawa grid C and no-slip boundary conditions on Arakawa grids B and E. Free-slip boundary conditions (or its modification) are probably more appropriate, however, Griffies and Hallberg [2000] refer that a natural formulation of free-slip on the B-grid does not exist. The grid configuration affects the design of the numerical schemes and their performance as we will discuss later.

The LSOMG-BT model provides four time-stepping schemes: The Euler implicit scheme (IMP), the modified Crank-Nicolson (CNmod) scheme [Campin et al., 2004], the forward-backward (FB) scheme [Gadd, 1974, Mesinger, 1977] (or its modification the predictor-corrector (PC) scheme) and the generalized forward-backward (FBgen) scheme [Shchepetkin and McWilliams, 2005, 2008]. However, the total number of spatio-temporal configurations available in the model is not 3×4 since some schemes are applicable at particular spatial grids only. The available model configurations are FB on the grid B, FB (or PC), FBgen and CNmod on the grid C and FB (or PC) and IMP on the grid E.

The model is forced by the wind blowing over the ocean surface and tides. The wind stress is calculated from the wind velocity at 10 m height. We use the bulk formula of [Trenberth et al., 1990, Timmermann et al., 2009]. The tidal force is expressed in terms of the second-degree tidal potential V_2. We consider the gravitational attraction of two celestial bodies, the Moon and the Sun. Their positions are found at each time step by the package of subroutines NOVAS F3.1 provided by the U.S. Naval Observatory [Kaplan et al., 2011].

The SWE in the barotropic tidal model needs to be supplemented with the self-attraction and loading term $\boldsymbol{\tau}_{sal}$ and the internal wave drag term $\boldsymbol{\tau}_{iwd}$. The self attraction and loading (SAL) describes the change of gravity field due to the deformation of the Earth's surface when the load is applied, due to the displacement of the Earth's masses when the load is applied and due to the self-gravitation of the load itself [Hendershott, 1972]. The LSOMG-BT model uses the so-called scalar approximation of SAL [Accad and Pekeris, 1978] in which $\boldsymbol{\tau}_{sal}$ is proportional to the SSH gradient,

$$\boldsymbol{\tau}_{sal} = \beta_s g \nabla \eta. \tag{6}$$

The coefficient β_s may in principle be spatially dependent but it is a constant in the LSOMG-BT model.

In the process of tidal dissipation, a part of the tidal energy is transferred from the barotropic to baroclinic tides. The baroclinic tides then propagate in the ocean interior in the form of internal waves and they are losing their energy when

breaking on rough topography. The $\boldsymbol{\tau}_{iwd}$ term has the form of a linear friction and so it is called the "internal wave drag" (IWD) or the "internal tide drag". The LSOMG-BT model implements the IWD scheme of Jayne and St. Laurent [2001]

For further details about the LSOMG-BT model, we refer to Sec. 4 of the thesis.

1.4 Baroclinic LSOMG model

The LSOMG model solves the primitive equations under the Boussinesq and hydrostatic approximations,

$$\mathbf{u}_{,t} + \nabla \cdot (\mathbf{v} \otimes \mathbf{u}) + M\mathbf{e}_3 \times \mathbf{v} = -f\mathbf{e}_3 \times \mathbf{v} - \frac{\nabla_h p}{\rho_0} + \mathbf{F}^{(\mathbf{u})}, \tag{7}$$

$$p_{,z} = -\rho g, \tag{8}$$

$$\nabla \cdot \mathbf{v} = 0, \tag{9}$$

$$C_{,t} + \nabla \cdot (\mathbf{v}C) = -\nabla \cdot \mathbf{F} + S^C, \tag{10}$$

$$\eta_{,t} = -\nabla_h \cdot \mathbf{U} + q_w, \tag{11}$$

where $\mathbf{v} = \mathbf{u} + w\mathbf{e}_3$ is the complete velocity vector, $\mathbf{u}$ is the horizontal velocity vector, w is the vertical velocity, M is the advective metric frequency, p is the pressure, ρ is the density of water, C is the tracer (temperature or salinity), $\mathbf{F}^{(\mathbf{u})}$ is the friction force, $\mathbf{F}$ is the turbulent tracer flux, S^C is the volume source of tracer C, q_w is the surface water flux, $a_{,z}$ denotes partial derivative of a with respect to the vertical coordinate z and ∇ is the three-dimensional (3-D) gradient operator.

We use the following boundary conditions at the surface,

$$w = \eta_{,t} - q_w, \tag{12}$$

$$q_w\mathbf{u} + A_V\mathbf{u}_{,z} = q_w\mathbf{u}_w + \frac{\boldsymbol{\tau}_w}{\rho_0}, \tag{13}$$

$$p = 0, \tag{14}$$

$$q_wC - \mathbf{F} \cdot \mathbf{N} = q_wC_w - V_{piston}\left(C_1 - C^{data}\right) + Q_C^{turb,0}, \tag{15}$$

at the bottom,

$$w = 0, \tag{16}$$

$$A_V\mathbf{u}_{,z} = \boldsymbol{\tau}_b, \tag{17}$$

$$\mathbf{F} \cdot \mathbf{N} = 0, \tag{18}$$

and at lateral boundaries,

$$\mathbf{u} \cdot \mathbf{N} = \mathbf{F}^{(\mathbf{u})} \cdot \mathbf{N} = \mathbf{F} \cdot \mathbf{N} = 0, \tag{19}$$

where q_w is the surface water flux, A_V is the non-negative vertical viscosity, V_{piston} is the piston velocity, C_1 is the tracer concentration in the ocean surface layer, C^{data} is data prescribed tracer concentration, $Q_C^{turb,0}$ is the turbulent flux from data or another model and $\mathbf{N}$ is the normal to the particular boundary.

The ocean bathymetry is derived either from GEBCO [IOC, IHO and BODC, 2003] or ETOPO1 [Amante, 2009] data. The initial and surface temperature and

salinity distributions are taken from the World Ocean Atlas 2013 [Locarnini et al., 2013, Zweng et al., 2013]. We use ERA-Interim [Dee et al., 2011] atmospheric data by default but we also tested CORE-II data [Large and Yeager, 2009].

It is beyond the scope of this summary to discuss the LSOMG model features in detail. We refer the interested reader to Sec. 5 of the thesis.

1.5 Tsunami and tidal numerical tests

The following study is published as a paper Šachl et al. [2020]. It is a result of cooperation with my colleague David Einšpigel, the author of the DEBOT model.

1.5.1 Introduction

The performance of hydrodynamic tidal models is limited by several factors such as the IWD, SAL, bottom drag coefficient, bathymetry precision and other numerical issues (e.g. splitting of tidal and non-tidal velocities and splitting of the barotropic and baroclinic systems). The study of Stammer et al. [2014] confirms that the accuracy of purely (no-data constrained) hydrodynamic barotropic models is significantly lower than the accuracy of assimilative models that are constrained by data. This means that if a pure hydrodynamic barotropic model is tested against real data, a bug in the numerical model may not be found. A simplified numerical test would be useful but it was not available.

Therefore, we propose a set of numerical tests suitable for a global OGCM forced by tides. We use these tests to inspect the performance of several time stepping schemes and computational grids which are used in the state-of-art OGCMs. Although the proposed numerical tests are simple compared to the realistic simulations, their analytic solutions are not available. We thus check the conservation of time invariants to ensure that the solution is physically meaningful. We also compare the time evolution of certain physical quantities and the differences in sea surface heights at particular time instants with respect to a reference solution.

1.5.2 Numerical setup

In total, six different configurations of the LSOMG-BT model are subject to the tsunami TSU test and the tidal tests TIDa and TIDb. We test FB on the grid B, FB, FBgen and CNmod on the grid C, and FB and IMP on the grid E, see Table 2. Note that these configurations are used in the following OGCMs: C–FB in MOM6 and HIM, C–FBgen in ROMS, C–CN in MITgcm, B–FB in MOM5, and E–IMP in LSG.

The horizontal friction and bottom stress are set equal to zero in the numerical tests, since we inspect the energy conservation and dissipative terms would violate it. Besides that, neither SAL nor IWD parameterizations are used in the tests. Both terms are needed for a realistic modelling of barotropic tides as discussed in Sec. 1.3 but they are pointless in the simplified tests. Note that the contribution of advection terms should not be significant in our numerical tests according to the results of tests carried out by the full nonlinear DEBOT model.

The initial conditions in the TSU test are given by zero velocities over the globe and a Gaussian-shape depression of the SSH with the maximum amplitude of 100 m. The ocean bottom is mostly flat but there is a Gaussian-shape mountain

Configuration	Grid	Time-stepping scheme	Ocean model
C–FB	C	Forward-backward (FB)	MOM6, HIM
C–FBgen	C	Generalized forward-backward (FBgen)	ROMS
C–CN	C	Modified Crank-Nicolson (CNmod)	MITgcm
B–FB	B	Forward-backward (FB)	MOM5
E–FB	E	Forward-backward (FB)	-
E–IMP	E	Euler implicit (IMP)	LSG

Table 2: Model configurations considered in the numerical tests and ocean models which use these configurations.

which arises from the ocean bottom. We prescribe two continents at the poles. We prefer the quasi global to the fully global setup since many OGCMs solve the problem of meridians converging at the North Pole by relocating coordinate poles to continents, and these OGCMs would be unable to run the fully global simulation. There is no external forcing, the only "forcing" in this test being the nonzero initial conditions.

The initial conditions in TIDa and TIDb are homogeneous, i.e., velocities and SSH are zero at time $t = 0$ s. The meridional boundaries are the same as in the TSU test. The initial positions of the Moon and Sun are given by their positions on January 1, 2015, 00:00:00 UTC. We apply space and time dependent tidal forcing to the initially resting ocean in the successive time steps. The tidal tests differ in their bathymetry and land-mask. In TIDa, the ocean bottom undulates with four Gaussian-shape ridges. In TIDb, the ocean bottom is flat and we prescribe a realistic land mask.

The spatial resolution of Arakawa grids B and C is chosen to be 0.5° for all numerical tests. The 0.5° resolution is sufficient for testing, the results do not change much when finer resolutions (1/3°, 1/4°) are used (not shown). The E-grid resolution is chosen to be $\Delta\lambda_E = \frac{3}{2}\Delta\lambda_C = 0.75°$.

The time step is chosen to be slightly below the Courant-number criterion in order to keep simulations stable for explicit schemes. We use the time step $\Delta t = 15$ s in all tests.

1.5.3 Results

The total volume of ocean water and potential-vorticity invariant are well conserved in all tested schemes and numerical tests. The energy conservation is violated in several model configurations. The implicit time-stepping scheme used in one model configuration suffers from the energy leakage. The leakage reaches 70% and 18% of energy in the TSU and TIDa numerical tests, respectively. We recommend not to use the implicit time-stepping scheme for tidally driven models, although the energy conservation is violated much less in the tidal numerical test than in the tsunami numerical test. The B-grid and E-grid model configurations do not conserve energy either if biharmonic smoothing of SSH is applied. The energy leakage reaches 2.1% and 8.2% in TSU and 4.6% and 4.1% in TIDb in B-grid and E-grid model configurations, respectively. It is probably an acceptable energy leakage for a global tidal model since its realistic configuration contains internal wave drag and bottom drag terms which are tuned to obtain realistic

results. All C-grid schemes conserve energy successfully. Regarding the spherical harmonic expansion coefficients, the largest coefficients in the TIDa solutions have degree l and order m equal to $l = 2$, $m = 2$ and $l = 4$, $m = 2$. The other significant coefficients have even degrees, which is a plausible result for a tidally driven numerical test.

There are differences between C-grid and B/E-grid solutions in all numerical tests, see, e.g., Figs. 1 and 2. Comparisons of spatial patterns and time curves show that discrepancies are more pronounced in the vicinity of domain boundaries as a consequence of different boundary conditions (free-slip and no-slip) and shapes of rigid boundaries on different Arakawa grids. The most distinct dis-

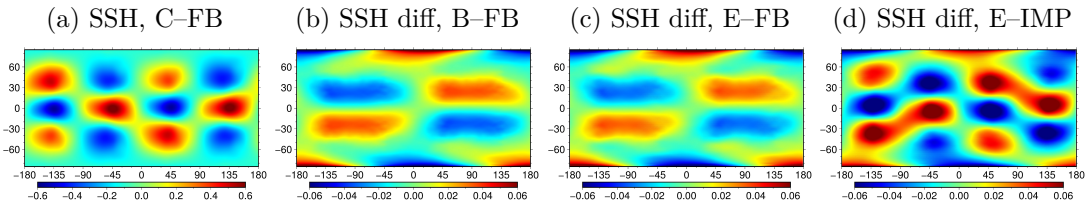

Figure 1: Panel (a) shows SSH [m] computed in the TIDa numerical test using the C–FB model configuration at day 13. The other panels show differences [m] between the SSH at panel (a) and the SSH computed using model configurations B–FB (b), E–FB (c) and E–IMP (d).

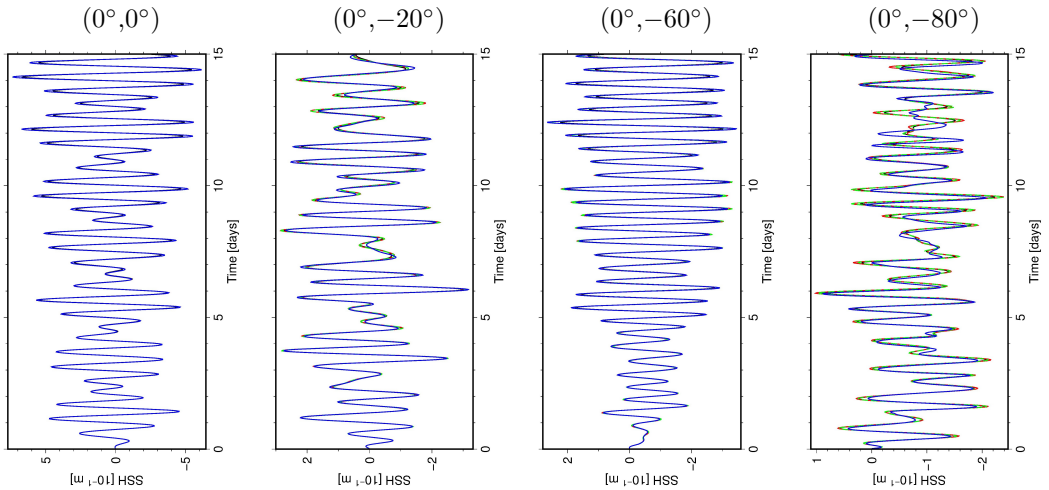

Figure 2: Time evolution of SSH at the chosen check points, see (λ, ϕ) above each panel, in the TIDa numerical test computed using model configurations C–FB (blue), B–FB (red), E–FB (green) and E–IMP (black)

crepancies are present in the TIDb numerical test in which boundary effects have a much stronger impact on the solution due to the significantly larger extent of land areas. Both free-slip and no-slip boundary conditions are approximations of the real-world boundary conditions, which are a combination of these two options. The choice of boundary conditions could be important, but it is beyond the scope of this study to test which one is closer to reality.

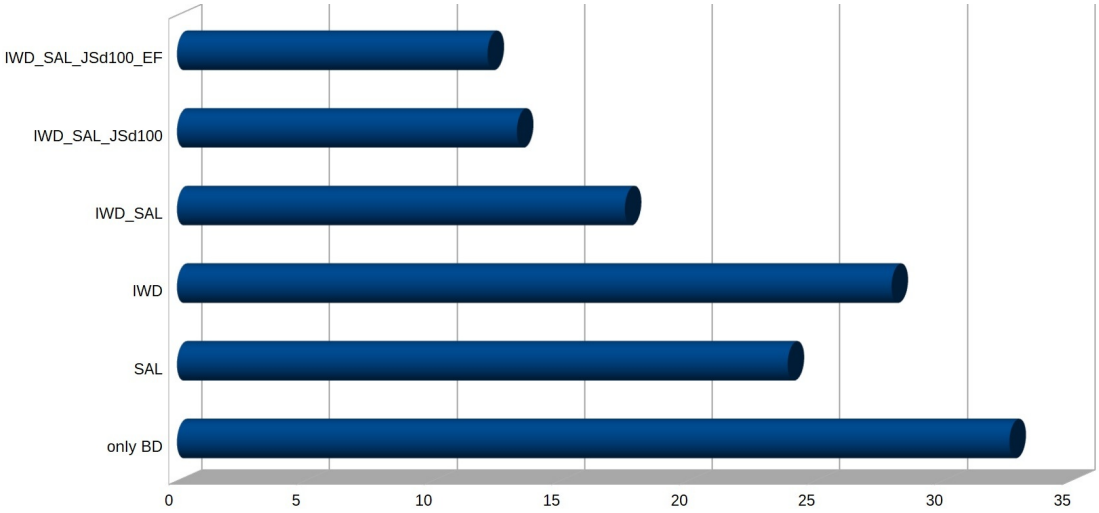

Figure 3: RSS [m] from the barotropic LSOMG-BT model in the validation experiment. Several model configuration are tested. The model is run with the bottom-drag (BD), internal wave drag (IWD), self-attraction and loading (SAL), nonlinear free surface (EF). Internal wave drag is applied if $H > 1000$ m (without JSd100) or if $H > 100$ m (with JSd100).

1.6 Tidal barotropic circulation

We validate the tidally driven circulation from the LSOMG-BT model by comparison with the commonly used and respected tidal model TPXO8-1. Our validation experiment is similar to the one performed by Buijsman et al. [2015]. We run the LSOMG-BT model for 19 days. The first 16 days serve as a spin up. According to our experience, it is a sufficiently long period to spin up a barotropic tidal model. The last three days are used to compare the SSHs from the LSOMG-BT and TPXO8-1 models. In our comparison, we consider only grid points where ocean is deeper than 1000 m. Additionally, the tides in high latitudes are not considered. The presence of sea ice makes the prediction of high-latitude tides complicated. Consequently, we restrict ourselves to $-66° < \phi < 66°$. Our metric is the so-called root-sum-square (RSS),

$$RSS = \sqrt{\frac{\left\langle \int\limits_A \left(\eta_{LSOMG} - \eta_{TPXO}\right)^2 dA \right\rangle}{A}}, \tag{20}$$

where A denotes the Earth's surface and the bracket denotes the time averaging. We choose the sampling frequency of tidal SSH to be 30 minutes and we average all samples stored during the last three days of our experiment.

The LSOMG-BT model is run in the 0.25° resolution with the time step $\Delta t = 7.5$ s. The coefficient of bottom friction is set to $C_b = 2.5 \times 10^{-3}$ and the horizontal viscosity is equal to $A_H = 1.25 \times 10^3$ m^2/s

The results of our experiment are depicted in Fig. 3. If only bottom drag is included and no tidal parameterizations are used, the RSS is rather large, $RSS =$ 32.62 cm. The inclusion of IWD or SAL improves the accuracy significantly which is in agreement with the conclusions of other authors. The RSS reduces down to 28.0 cm and 23.93 cm if we include IWD or SAL, respectively. Thus, the

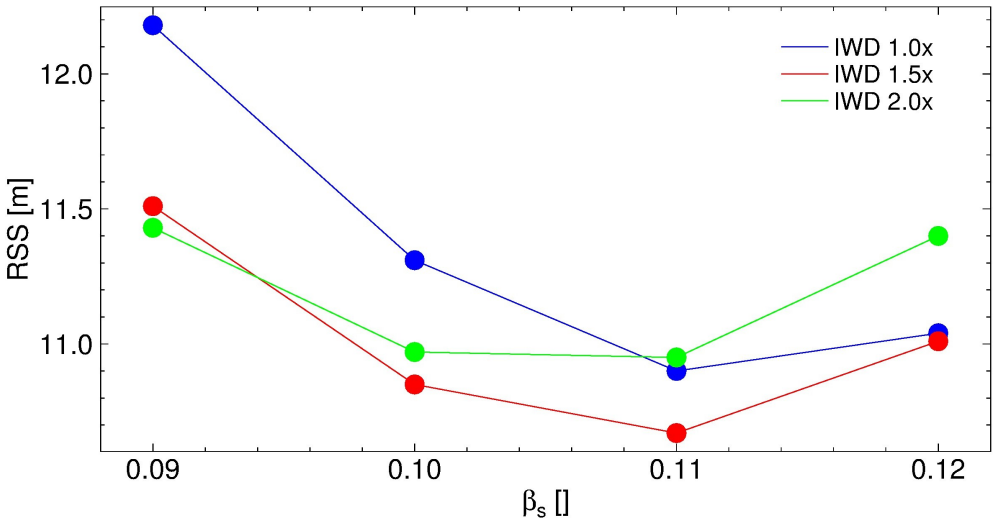

Figure 4: Sensitivity of RSS in the tidal validation experiment on the values of IWD and SAL.

parameterization of SAL affects the SSH more than the parameterization of IWD in our experiment. Jayne and St. Laurent [2001] applied the IWD only in waters deeper than 1000 m. We also used this setting but we also tried to relax this condition to waters deeper than 100 m. Our results suggest that the condition $H > 100$ m for the application of IWD is better than the condition $H > 1000$ m, the RSS has improved from 17.55 cm to 13.32 cm. This finding is in agreement with Arbic et al. [2004] but it is in disagreement with Buijsman et al. [2015] who strongly supported the condition $H > 1000$ m. Finally, the nonlinear free surface outperforms linear free surface, although the improvement of RSS is only modest, from 13.32 cm to 12.17 cm. However, it is expected that the improvement would be larger if we focused on shallow regions.

We further study sensitivity of the RSS to the strength of IWD and SAL. We test three IWD setups: The default setup, the setup with IWD increased 1.5× and the setup with IWD increased 2×. And four values of β_s coefficient in the SAL parameterization: 0.09 (default value), 0.10, 0.11 and 0.12. In total, we computed RSS for 12 setups. The results are depicted in Fig. 4. The computed RSS indicates that increased IWD strength and larger β_s are favourable. On the other hand, $\beta_s = 0.12$ is obviously too large value since the RSS increases for all three IWD setups if β_s is increased from $\beta_s = 0.11$ to $\beta_s = 0.12$. Similarly, 2× increased IWD is too strong since the RSS computed with 1.5× increased IWD is smaller for all tested values of β_s, except for the default $\beta_s = 0.09$ where it is slightly larger. The best $RSS = 10.67$ cm is achieved with 1.5× increased IWD and $\beta_s = 0.11$. Similar but slightly larger $RSS = 10.85$ cm is achieved with 1.5× increased IWD and $\beta_s = 0.10$ and $RSS = 10.90$ cm is achieved with the default IWD and $\beta_s = 0.11$.

1.7 Steady wind-driven barotropic circulation

We follow Frisius et al. [2009] and perform barotropic simulations forced by the annual-mean wind stress. Frisius et al. [2009] used the SOM model forced by wind stresses of Hellerman and Rosenstein [1983]. We do not have this data and

therefore we use ERA-Interim data [Dee et al., 2011]. The annual means of zonal and meridional wind velocities are not available in the ERA-Interim archives. We compute the annual means by averaging the monthly means from the year 2013. We perform two experiments in accordance with Frisius et al. [2009]. The experiments differ in the bathymetry used. The bathymetry is realistic in the first experiment and there is a flat bottom in depth of 5000 m in the second experiment. We run the simulations for 90 days in accordance with Frisius et al. [2009]. We checked out that it is a sufficiently long spin up. In fact, the spin-up could be shorter in the experiment with the realistic bathymetry.

The results are depicted in Fig. 5. Panels (a,c) correspond to the experiment with the realistic bathymetry, panels (b,d) correspond to the experiment with the flat bathymetry. We test two viscosity values. The smaller value $A_H = 2\times10^4$ m/s^2 is used in panels (a,b) while one-order larger value $A_H = 2\times10^5$ m/s^2 is used in panels (c,d). The SOM results are depicted in Fig. 6 (a,b) and the GECCO reanalysis is shown in Fig. 6 (c).

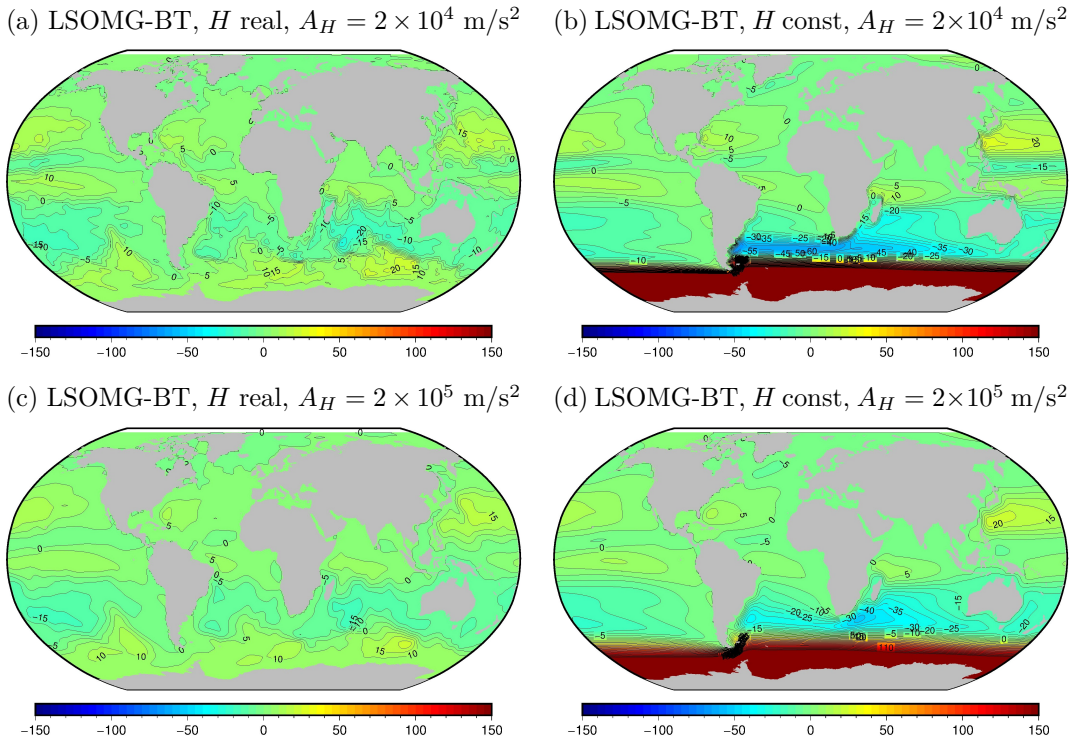

Figure 5: Barotropic stream function [Sv] from the LSOMG-BT wind-driven barotropic simulations. Bathymetry used in simulations is either realistic (a,c) or constant (b,d), $H = 5000$ m. The viscosity used is either $A_H = 2\times10^4$ m/s^2 (a,b) or $A_H = 2\times10^5$ m/s^2 (c,d).

An important finding, which does not depend on the viscosity used and it is in agreement with the SOM results, is that the barotropic modelling of the ACC current is inaccurate. If the bathymetry is realistic, the ACC current virtually disappears. In contrast, if the bathymetry is flat, the ACC current is about five times stronger than it actually is. It is known that the baroclinic processes are important for the ACC current [Olbers and Lettmann, 2007, Cunningham et al., 2003]. The barotropic model does not contain baroclinic pressure gradients and

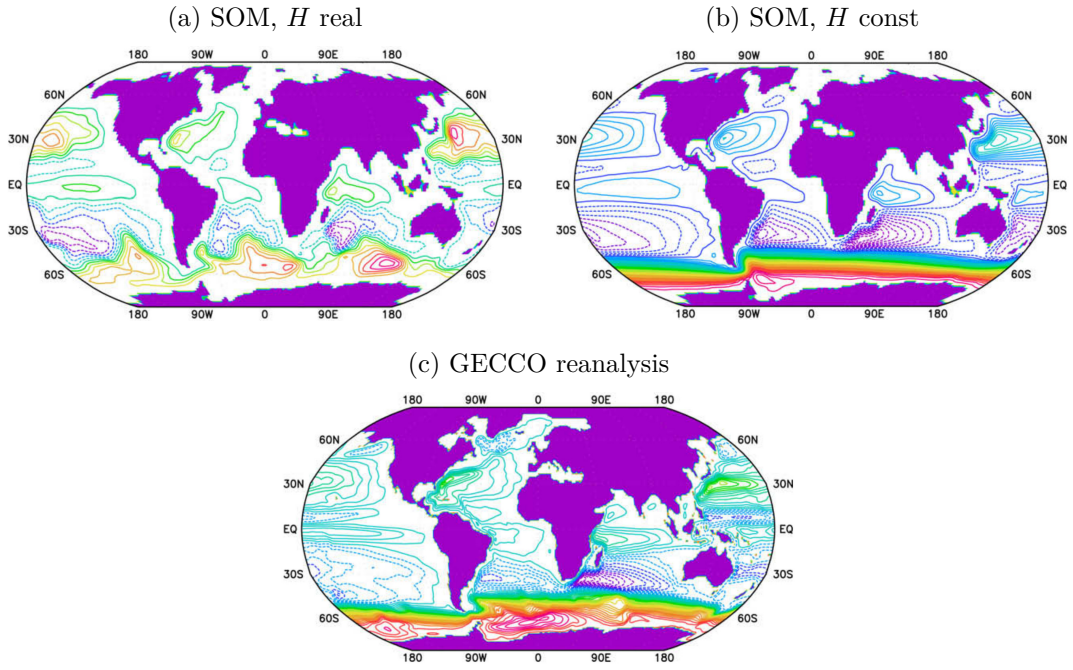

Figure 6: Barotropic stream function [Sv] from the SOM wind-driven barotropic simulations (a,b) and the GECCO reanalysis (c). Stream lines are depicted in 5 Sv intervals, negative stream lines are dashed. Bathymetry used in simulations is either realistic (a) or constant (b), $H = 5000$ m.

thus an important part of the ACC dynamics is missing in the barotropic model.

The absence of strong ACC current in the experiment with realistic bathymetry affects currents in the Southern hemisphere. The stream functions of these currents computed in the LSOMG-BT and SOM models do not match the GECCO stream functions. The situation is different in the Northern hemisphere where the computed stream functions are in much better agreement with the GECCO stream functions. The stream functions are similar in both experiments, but they are notably smoother in the flat-bottom experiment. In fact, it seems that they are overly smooth if we compare them with GECCO.

In terms of viscosity, the LSOMG-BT stream functions are smoother and the flow is weaker if higher viscosity is used. The LSOMG-BT high-viscosity results are in better agreement with the SOM results despite the fact that viscosity $A_H = 2 \times 10^5$ m/s^2 is rather large for a 1° model. However, the GECCO results indicate that the low-viscosity setup is more correct.

The LSOMG-BT and SOM stream functions have similar shapes but the flow is stronger in the SOM model. As already mentioned, the forcing is not identical in both models. In order to assess the influence of a different forcing data set, we repeat all LSOMG-BT simulations with the CORE-II forcing. The resulting stream functions are shown in Fig. 7. The flow is noticeably more vigorous in the CORE-II simulations. We assess that the transports are larger in the CORE-II simulations by 10-15 Sv than in the ERA-Interim simulations.

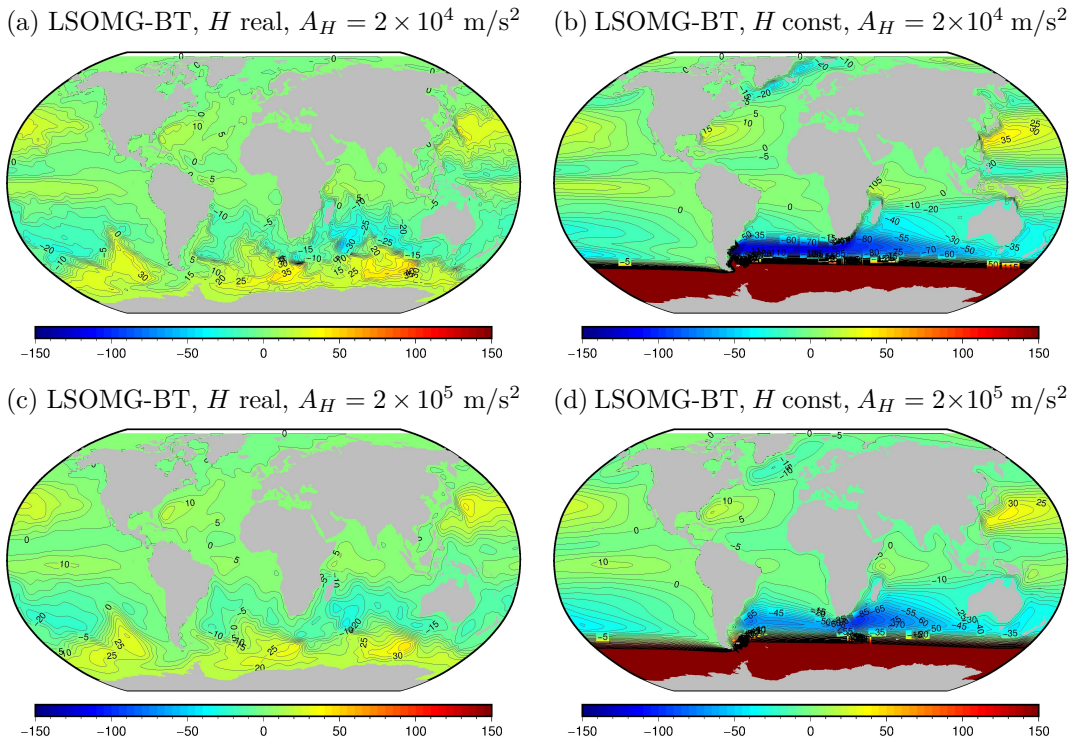

Figure 7: The same as Fig. 5 but the simulations are forced by the CORE-II instead of ERA-Interim wind stresses.

1.8 Wind driven baroclinic circulation

In Sec. 1.7, we demonstrated that the barotropic model can reasonably model the wind-driven driven gyres on the northern hemisphere but it completely fails to model the ACC current which significantly affects the circulation on the southern hemisphere. Consequently, we switch to the baroclinic LSOMG model in this section. We shall inspect the model SSH, barotropic transports, barotropic stream function and globally averaged temperature and salinity.

In all the presented simulations, we use the horizontal Smagorinsky viscosity [Smagorinsky, 1963, 1993] with the minimum viscosity based on the grid Reynolds number. The vertical viscosity is constant $A_V = 1 \times 10^{-3}$ m^2/s. The nonlinear bottom friction with $C_b = 2.5 \times 10^{-3}$ is used. We use depth-dependent horizontal (epineutral) and vertical (dianeutral) diffusivities of Bryan and Lewis [1979] type. We use the Lax-Wendroff scheme with flux limiters according to Smith et al. [2010] for the advection of tracers. The energy conserving scheme ENE [Madec, 2012] is used for the discretization of the Coriolis term together with the divergence damping of the second-order. The convective adjustment scheme of Rahmstorf [1993] is applied. The predictor-corrector time stepping scheme is used in the barotropic system. The horizontal model resolution is 1° and we use either 11 or 22 layers in the vertical. The model time step is 30 minutes for the baroclinic system and 30 s for the barotropic system. The simulations are 21 years long. The first 20 years serve as a spin-up. The annual means are computed from the last year of the simulation.

We start with the simulations from the 11-layer LSOMG model forced by climatological ERA-Interim wind stresses and surface fluxes prescribed in the form

of strong 30-day relaxation towards the surface temperature and salinity. Despite the simplified surface forcing and somewhat coarse resolution in the vertical, the model can produce reasonable results.

Fig. 8 (a) shows the SSH computed in the LSOMG model. For comparison, the SSHs from the ECCO and POP models are depicted in Fig. 8 (b) and (c), respectively, and the SSH estimate of Maximenko et al. [2009] derived from satellite and marine data is depicted in Fig. 8 (d). Note that the ECCO product combines the 1° MITgcm model with the data to obtain the best SSH estimate. The POP model used much higher horizontal resolution of 0.1° but it was a purely hydrodynamic simulation as in our case.

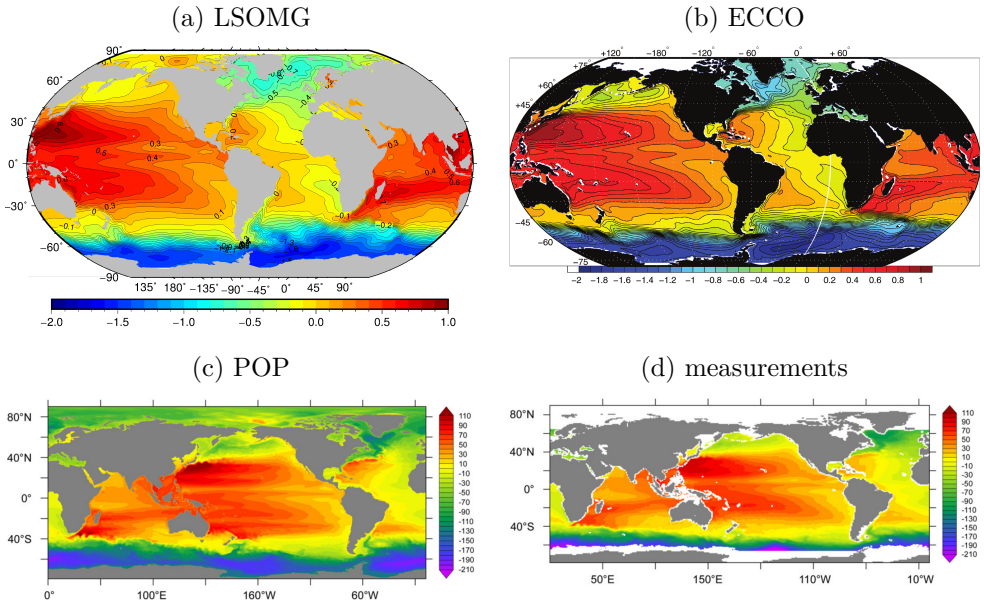

Figure 8: SSHs [m] computed using the LSOMG (a), ECCO (b), and POP (c) models and the SSH determined from satellite and marine data (d). Panel (b) is taken from Wunsch [2011], panels (c,d) are taken from McClean et al. [2011].

Overall, the SSH from the LSOMG model matches the other solutions very well. The SSH has its typical pattern with large-scale lobes in the ocean basins especially in the Pacific Ocean. In details, the SSH from the LSOMG model displays certain deficiencies, e.g., the SSH is underdeveloped in the South Atlantic and certain distortion is present also in the North and South Pacific. Nevertheless, the SSH from the POP model also displays deviations from the ECCO estimate and data-derived SSH of Maximenko et al. [2009]. We thus consider the LSOMG result as satisfactory.

We further inspect the vertically integrated currents. Fig. 9 shows the velocity vertically integrated from the surface down to approximately 1000 m in the LSOMG and OMCT models. Both simulations are in a good agreement, we can see the ACC current, the equatorial currents and the boundary currents in the ocean basins. The OMCT currents seems to be weaker than the LSOMG currents. This is notable on the ACC current and the western-boundary current in the South Atlantic which is pronounced in the LSOMG simulation but it is hardly visible in the OMCT simulation. We argue that the weaker flow in the OMCT simulation could be caused by its resolution. The OMCT used 13 layers in the

vertical which is similar to the LSOMG simulation but the horizontal resolution was only 1.875°.

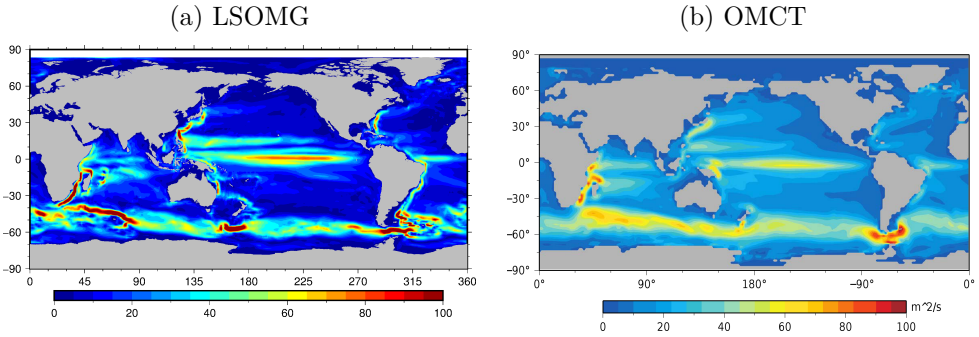

Figure 9: Vertically integrated velocity [10^3 m^2/s] computed using the LSOMG (a) and OMCT [Irrgang et al., 2016a] (b) models.

The comparison with the OMCT could lead us to conclusion that the flow in the 11-layer LSOMG simulation with simplified forcing is overly strong. This not true. We will show that it is weaker than it should be.

Fig. 10 shows barotropic stream functions from the MASNUM [Lei, 2014] and CNRM-CM5.1 [Voldoire et al., 2013] models. The MASNUM model was used in the ocean-only 0.5° configuration with 21 layers in the vertical. The CNRM-CM5.1 is a coupled atmosphere-ocean model with the nominal horizontal resolution of 1° which is refined in the tropics to 1/3° and 42 vertical levels.

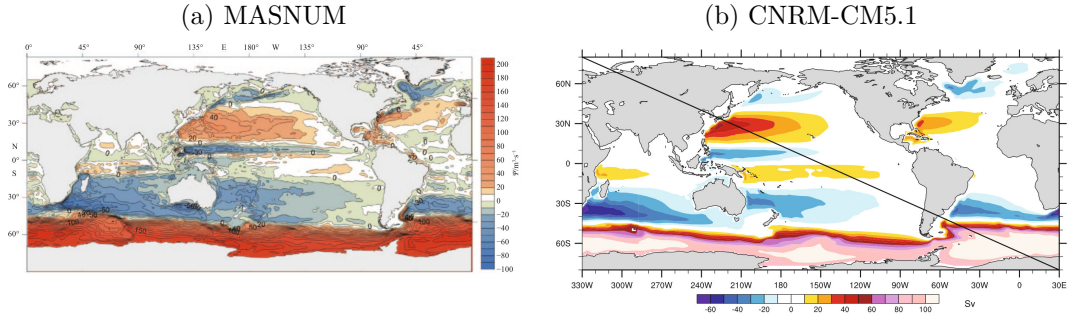

Figure 10: Barotropic stream functions [Sv] from the MASNUM [Lei, 2014] (a) and CNRM-CM5.1 [Voldoire et al., 2013] (b) models.

Fig. 11 (a) depicts the barotropic stream function from the 11-layer LSOMG simulation with the simplified forcing. The LSOMG stream function is comparable with the MASNUM and CNRM-CM5.1 stream functions in terms of shape, however, it is globally weaker. It is well pronounced in the ACC region, where the MASNUM simulation is notably stronger. The ACC strength in this LSOMG configuration and the CNRM-CM5.1 model are comparable but the ACC current is underestimated in the CNRM-CM5.1 model [Voldoire et al., 2013].

In order to improve the simulation quality, we increase the vertical resolution from 11 to 22 layers, see Fig. 11 (b). The ACC strength has increased by approximately 10 Sv. The stream function has also increased in the North Pacific but also decreased in the North Atlantic and in the Indian Ocean. Overall, the

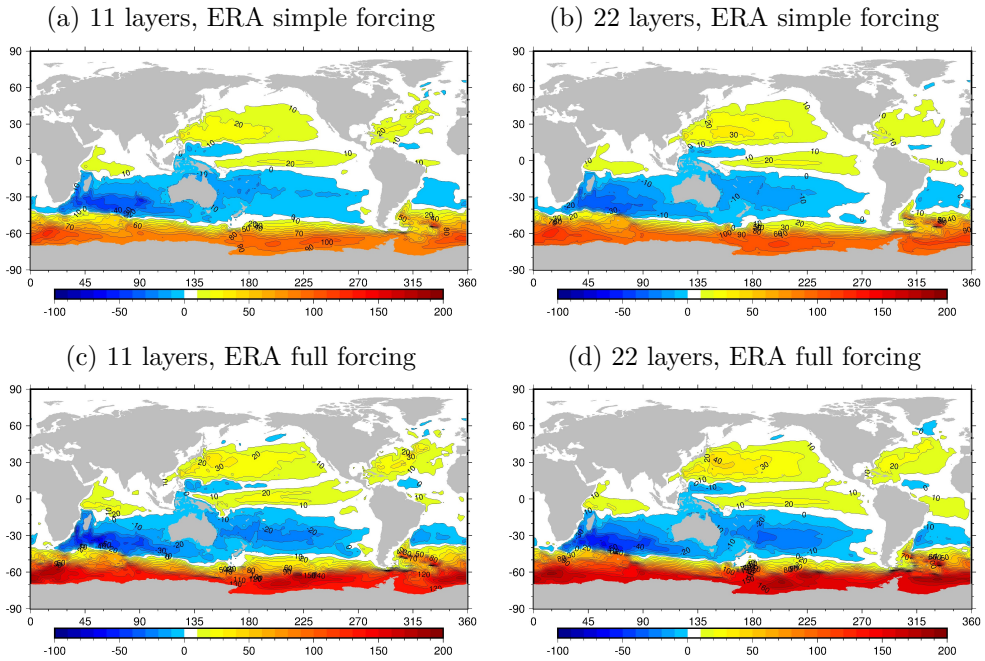

Figure 11: Barotropic stream functions [Sv] from the LSOMG simulations forced by ERA-Interim data.

stream function in the 22-layer simulation is not significantly better than in the 11-layer simulation.

In the next step, we improve the model forcing. We replace the simplified forcing by the full forcing. The major improvement is that the full forcing contains the proper heat fluxes computed using the bulk formulas of Large and Yeager [2004, 2009]. Additionally, the full forcing varies more rapidly in time since it is represented by daily values rather than monthly values in the simplified forcing. Fig. 11 (c) depicts the barotropic stream function from the 11-layer simulation with the full forcing. The improved forcing has a favourable impact on the stream function, all gyres are stronger. The major change is the strengthening of the ACC current. The stream-function maximum has increased from 126 Sv with the simplified forcing to 182 Sv with the full forcing. If we further increase the vertical resolution to 22 layers, the stream-function maximum is virtually the same with 184 Sv but the ACC current has further strengthened in most regions, see Fig. 11 (d). The stream function has also increased in the Pacific Ocean. This is favourable in terms of comparison with the MASNUM, CNRM-CM5.1 and GECCO (see Fig. 6 (c)) stream functions but also with the altimeter estimate of 42 Sv of Imawaki et al. [2001]. The steam function in the Atlantic Ocean is well shaped but it remains to be slightly underdeveloped. For example, the strength of the Florida current should be around 30 Sv according to Schott et al. [1988].

We also test the sensitivity of presented stream functions on the particular forcing data set. We replace the ERA-Interim forcing with the CORE-II forcing and repeat the simulations. The corresponding stream functions are depicted in Fig. 7.14 in the thesis. The CORE-II stream functions in the simulations with the simplified forcing are stronger than the corresponding ERA-Interim stream functions. The differences over 10 Sv are present in the North Pacific and Indian

Oceans. The stream-function maximum has increased from 126 Sv to 155 Sv in the 11-layer simulations and from 134 Sv to 160 Sv in the 22-layer simulations. This corresponds to the wind-driven barotropic simulations presented in Sec. 1.7. However, in contrast to the ERA-Interim simulations, the CORE-II simulations with the full forcing are not that much different to the CORE-II simulations with the simplified forcing. The major differences are the strengthening of the ACC current. The CORE-II simulations with the full forcing match the corresponding ERA-Interim simulations well. The ERA-Interim stream functions are in slightly better agreement with the MASNUM, CNRM-CM5.1 and GECCO stream functions but the differences are relatively small.

Finally, we inspect the globally averaged temperature and salinity in the presented simulations. Fig. 12 (a,c) show the globally averaged temperature in the ERA-Interim and CORE-II simulations, respectively. Fig. 12 (b,d) show the globally averaged salinity in the ERA-Interim and CORE-II simulations, respectively. In all panels, the red curves correspond to the simulations with the simplified

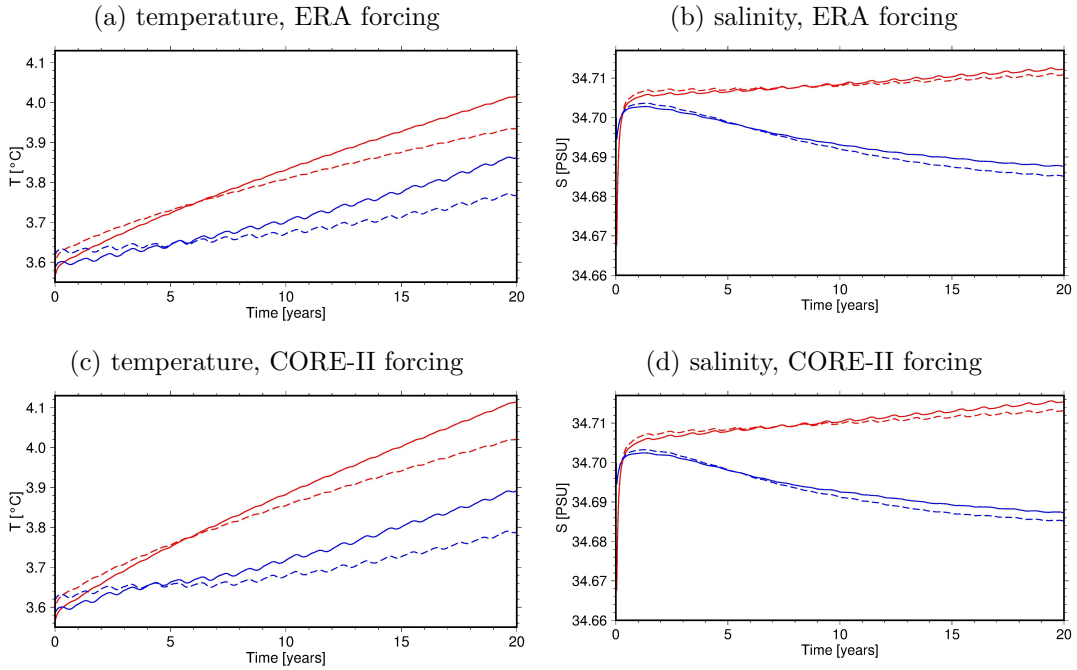

Figure 12: Globally averaged temperature and salinity. Results from the 11-layer (solid curves) and 22-layer (dashed curves) simulations with the simplified (red curves) or full (blue curves) forcing.

forcing and the blue curves correspond to the simulations with the full forcing. The solid curves correspond to the 11-layer simulations and the dashed curves correspond to the 22-layer simulations. Overall, there are certain trends in the globally averaged fields. It is probably a model deficiency rather than a real phenomenon. The global temperature is better conserved in the 22-layer simulations than in the 11-layer simulations. Similarly, the simulations with the full forcing conserve temperature better than the simulations with the simplified forcing. The temperature increased by 0.42° and 0.52° in the 11-layer simulations with the simplified ERA-Interim and CORE-II forcings, respectively. That is a relatively large change. On the other hand, the temperature increased by 0.14° and

0.16° in the 22-layer simulations with the full ERA-Interim and CORE-II forcings, respectively. A comparable drifts were present in the simulations from the comparison study of Griffies et al. [2009]. The salinity trends are smaller than the temperature trends which is in accordance with the simulations in Griffies et al. [2009]. The figures are slightly misleading since there is a sharp decrease in salinity at the beginning of each simulation. The decrease is larger in the simulations with the simplified forcing. Consequently, the difference between the final and initial salinity is actually smaller in simulations with simplified forcing. It is almost zero in the ERA-Interim simulation and 0.003 PSU in the CORE-II simulation. There is a decrease in salinity of about 0.025 PSU in both 22-layer simulations with the full forcing. All values are acceptable.

2 Modelling of ocean-induced magnetic field

2.1 Introduction

The seawater is a conductive fluid which is flowing in the presence of the Earth's magnetic field (primary field). Consequently, a secondary magnetic field driven by the ocean currents is induced via the process of electromagnetic induction (EM).

The first attempts to numerically model the OIMF were by Stephenson and Bryan [1992], Flosadóttir et al. [1997] and Tyler et al. [1997] which were later followed by Vivier et al. [2004], Manoj et al. [2006] and others. All studies found a small (≈ 1 nT) signal at satellite height with the Antarctic Circumpolar Current (ACC) producing the largest signal because of its substantial water transport (it is the largest ocean current on Earth) and proximity to the geomagnetic pole.

Practical motivation for our research comes from the ongoing geomagnetic field measuring satellite mission, Swarm. One of the declared objectives of the mission – detecting magnetic signatures due to ocean circulation [Friis-Christensen et al., 2006] – has not yet been achieved. It is a challenging task. Firstly, the OIMF is overlaid by larger contributions ($\approx 50,000$ nT) from the main magnetic field and the magnetic fields of ionosphere and magnetosphere origin. Secondly, the OIMF may be erroneously attributed to the lithospheric field which is stationary in time and has comparable magnitudes. Nonetheless, if the ocean-induced contribution is one day reliably isolated from satellite magnetic data, it could constrain ocean dynamics [Irrgang et al., 2017]. Accurate and efficient modelling is necessary for this breakthrough.

2.2 Governing equations

The OIMF $\mathbf{B}(\mathbf{r}, t)$ obeys the quasi-static Maxwell equations supplemented by Ohm's law,

$$\nabla \cdot \mathbf{B} = 0, \tag{21}$$

$$\nabla \times \mathbf{B} = \mu_0 \left(\mathbf{j} + \mathbf{j}^{\mathrm{imp}} \right), \tag{22}$$

$$\nabla \times \mathbf{E} = -\frac{\partial \mathbf{B}}{\partial t}, \tag{23}$$

$$\mathbf{j} = \sigma \mathbf{E}, \tag{24}$$

where $\mathbf{E}(\mathbf{r},t)$ is the electric field, $\mathbf{j}(\mathbf{r},t)$ is the electric current density, $\mathbf{j}^{\text{imp}}(\mathbf{r},t)$ is the imposed electric current density, $\sigma(\mathbf{r})$ is the electric conductivity, μ_0 is the permeability of vacuum, $\mathbf{r}$ is the radius vector and t is time.

Alternatively, we can combine Eqs. (22)-(24) into the second-order EM induction equation for the OIMF,

$$\nabla \times \left(\frac{1}{\sigma}\nabla \times \mathbf{B}\right) + \mu_0 \frac{\partial \mathbf{B}}{\partial t} = \mu_0 \nabla \times \mathbf{E}^{\text{imp}}, \tag{25}$$

where $\mathbf{E}^{\text{imp}}(\mathbf{r},t)$ is the imposed electric field that is linked to the imposed electric current density through Ohm's law.

Note that Eqs. (21), (22) and (25) implicitly assume that the main geomagnetic field $\mathbf{B}_M(\mathbf{r},t)$ is a potential field and its temporal variations are much slower than the temporal variations of the OIMF.

The imposed electric field or electric currents are computed from the ocean velocity $\mathbf{u}(\mathbf{r},t)$ and the main geomagnetic field, following:

$$\mathbf{E}^{\text{imp}} = \mathbf{j}^{\text{imp}}/\sigma = \mathbf{u} \times \mathbf{B}_M, \tag{26}$$

where we assume that the main geomagnetic field is much stronger than the OIMF.

2.3 Physical approximations and numerical issues

The following study is a result of cooperation with our colleagues from GFZ, DIAS, Freie Universität Berlin and CIRES. We are concerned with modelling the OIMF due to the wind- and buoyancy-driven ocean circulation and inspect how various commonly used approximations affect the accuracy of modelled OIMF. The study was published as a paper [Šachl et al., 2019]. The tidally-driven OIMF is considered separately in a companion paper of Velímský et al. [2018].

[Šachl et al., 2019] originally summarized a benchmark study with different EM induction solvers involved but the paper was rejected. We thus modified our study. We present the results from the UTSM solver that was operated by the GFZ group in the paper. The performance of our UTSM solver that is described in Sec. 8.2.3 and Appendix G of the thesis is equal. It was simply not meaningful to present the results from both solvers since it was not a benchmark study any longer. Similarly, we used the ocean circulation calculated by the OMCT model that was operated by the GFZ group. We preferred OMCT to LSOMG since the model has already been used in the OIMF studies (e.g. Irrgang et al. [2016a,b], Saynisch et al. [2016]) and so it is known in the community.

2.3.1 Numerical setup

We use three EM induction solvers: the ElmgTD, X3DG and UTSM. All of them were thoroughly tested; ElmgTD and X3DG took part in the benchmark study of Kelbert et al. [2014], and were used to model OIMF in the past [Manoj et al., 2006, Irrgang et al., 2016a, Velímský et al., 2019]. The main characteristics of individual solvers are summarized in Table 4.

We consider four test cases labeled A-D which are summarized in Table 3. Complexity increases from Case A to Case D. In the simplest Case A, the underlying mantle is treated as a perfect insulator and the ocean has no vertical

	A	B	C	D
Mantle + core	insulator	1-D	1-D	1-D
Galvanic coupling	no	yes	yes	yes
Ocean layers	1	1	5	5
Self-induction	no	no	no	yes
EM solvers used	ElmgTD, X3DG, UTSM	ElmgTD, X3DG	ElmgTD, X3DG	ElmgTD

Table 3: Test cases considered in the study.

structure. In ElmgTD and X3DG, we use a single oceanic layer of finite thickness. The UTSM solver uses the equivalent thin-sheet setup. The test case is stationary and calculates a single snapshot corresponding to 2007/01/01. The solution is also unimodal, containing only the poloidal magnetic field.

In Case B, we include the 1-D mantle conductivity model of Grayver et al. [2017], and the core is considered to be highly conductive (10^4 S/m). We also consider a bimodal solution, the toroidal magnetic field is included. Thus, the ocean and mantle are galvanically coupled through vertical electric currents. The UTSM is not used anymore, as the physical model is beyond its approximation. The inclusion of galvanic coupling is very cheap for both the ElmgTD and X3DG solvers. The additional cost results in extension of runtime by a few percents.

In Case C, we add the vertical stratification of imposed currents and ocean conductivity, using five layers with lower boundaries at depths of 87.5 m, 187.5 m, 500 m, 1700 m and 6000 m. Runtimes of both the X3DG and ElmgTD solvers scale up from approximately one hour for Cases A and B to about one day for Case C.

Finally, Case D implements self-induction and we calculate the full time series throughout the year 2007. X3DG could theoretically solve this case by using a Fourier-transformed excitation in the frequency domain, but this is beyond the scope of our study since the OIMF's spectrum is wide ranged and the X3DG computation would be expensive. Given the cross validation of ElmgTD and X3DG on the static cases, we find it sufficient to use only ElmgTD to evaluate the effect of self-induction.

In all test cases, we consider the 3-D conductivity, σ, in the surface 6 km thick layer. We use $\sigma_{\text{ocean}} = 3.2$ S/m and $\sigma_{\text{crust}} = 10^{-3}$ S/m for the nominal conductivities of sea water and crust, respectively.

We simulate the general ocean circulation using the Ocean Model for Circulation and Tides [OMCT, Thomas et al., 2001]. The corresponding ocean velocities $\mathbf{u}$ build the source for ocean circulation's electric currents and the motional induction. We use the configuration in which OMCT is set up on a C-grid [Arakawa and Lamb, 1977] with a horizontal resolution of 1°, 20 layers in the vertical, and a time step of 20 minutes [Dobslaw et al., 2013]. We force the ocean model with 3-hourly reanalysis products from the European Centre for Medium-Range Weather Forecasts [ECMWF, Dee et al., 2011]. Ocean tides are not considered.

Each of tested EM solvers uses a different modelling technique – including different spatial discretizations and different ways to propagate dependent variables in time. Consequently, the resolution used is not exactly the same. We use 1°

	ElmgTD	X3DG	UTSM
Physics	full	full	UTSA
Ocean layer	3-D	3-D	2-D thin sheet
Sub-ocean layer	cond/insul	cond/insul	insul
Domain	time	freq	time
Lateral discretization	SH	PWC	FD+SH
Radial discretization	FE	PWC	-

Table 4: Quick comparison of the EM induction solvers used in the study. UTSA = unimodal thin-sheet approximation of Tyler et al. [1997] and Vivier et al. [2004] with insulating mantle and core, SH = spherical harmonics, FE = finite elements, PWC = piece-wise constant representation, FD = finite differences.

resolution in X3DG and UTSM. In ElmgTD, we set up the maximum spherical-harmonic degree to $j_{\max} = 480$ in Cases A-C in order to minimize the effect of ringing. In Case D, the solution evolves in time which forced us to decrease the resolution to $j_{\max} = 80$ in order to enable the use of the ElmgTD direct solver.

2.3.2 Results

The galvanic coupling is important for the modelling of wind-driven OIMF. Its omission affects the power spectrum, OIMF at the surface and OIMF at 6 km depth where especially Y component is affected, see Figs. 13 (compare Cases A and B), 14 (top row) and 15 (top row).

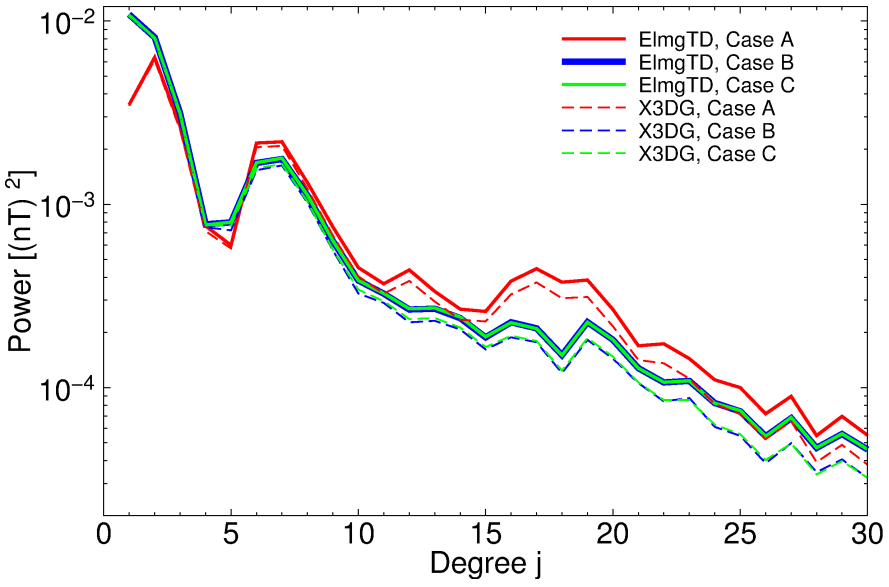

Figure 13: Power spectra of the OIMFs computed using the ElmgTD solver (solid line) and the X3DG solver (dashed line) in Cases A-C at the Earth's surface.

The self-induction is less important but it also matters. Fig. 16 shows that it affects lower spherical harmonic degrees (up to 40% of the spectral power on degree one) by damping sudden changes in the OIMF which results in a smoother evolution in time.

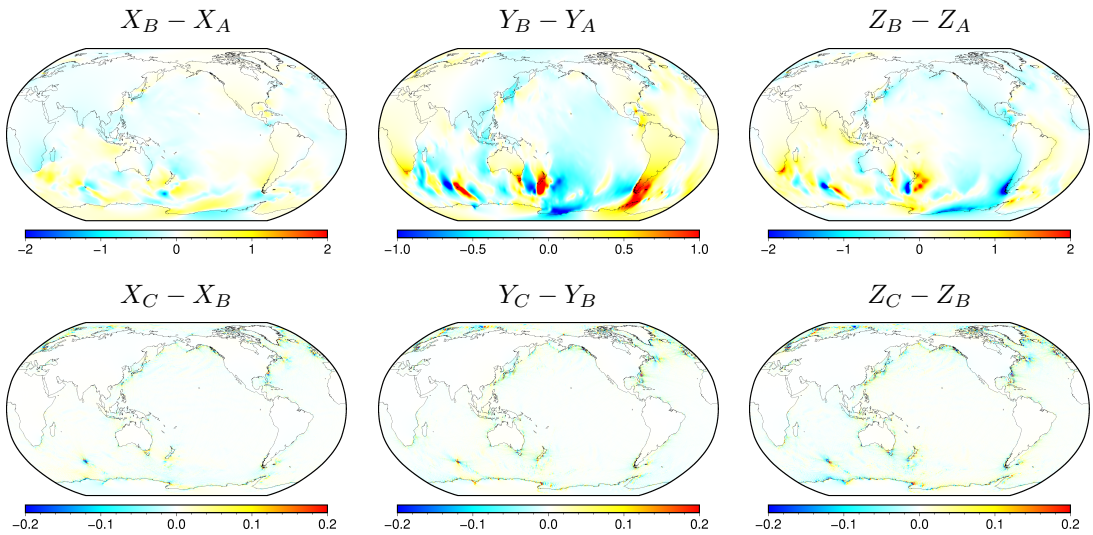

Figure 14: Effect of galvanic coupling (Case B) and vertical stratification (Case C) on the OIMF at the Earth's surface. Top row: Differences [nT] between Cases B and A in the X, Y, and Z components of the OIMFs from the ElmgTD solver. Bottom row: Differences between the OIMFs in Cases C and B.

One layer in the vertical is sufficient for global studies of OIMF, see Figs. 14 (bottom row) and 15 (bottom row). The local studies should consider a higher vertical resolution since it may locally cause the OIMF differences around 0.1 nT in the X and Y components and 0.15 nT in the Z component. We do not recommend to use unimodal thin sheet approximation of Tyler et al. [1997] and Vivier et al. [2004] since it neglects both galvanic coupling and self-induction. We recommend to use the horizontal resolution of at least 1°.

Conclusions

This thesis combines two different scientific fields: the oceanography and Earth magnetism. The first one was a real challenge for us. The numerical modelling of ocean circulation is well established in many seaside countries around the world. There is neither an oceanographic center nor a senior scientist working in oceanography in the Czech Republic. Additionally, OGCMs are results of colaborative work of research teams rather than individuals (which is more common in geophysics). Despite that, we have developed our OGCM rather than used an already existing one. We call it LSOMG. The LSOMG model is not revolutionary, but it is a decent work horse for the modelling of OIMF, which is the second part of this PhD. Moreover, developing the model from scratch required to study the numerical cores of state-of-art OGCMs and also to implement the numerical schemes on our own rather than take the model as a black box. It was a valuable experience.

The LSOMG model is 3-D baroclinic model but it can also be used in its simplified 2-D barotropic version called LSOMG-BT. LSOMG-BT is based on the shallow water equation which are discretized using the finite difference method. The model supports several time stepping schemes and Arakawa grids B, C and

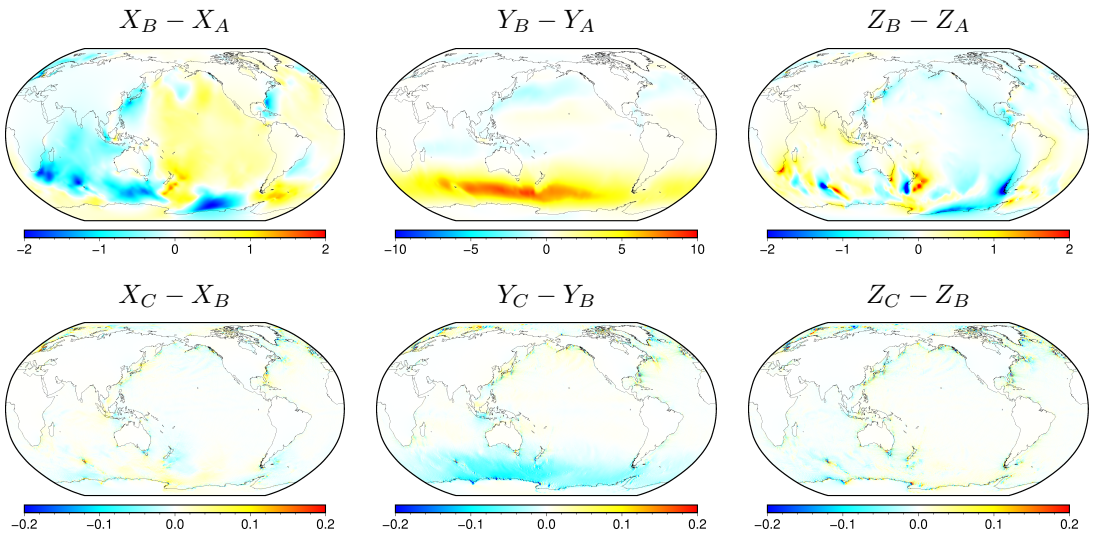

Figure 15: The same as Fig. 14 but at 6 km depth.

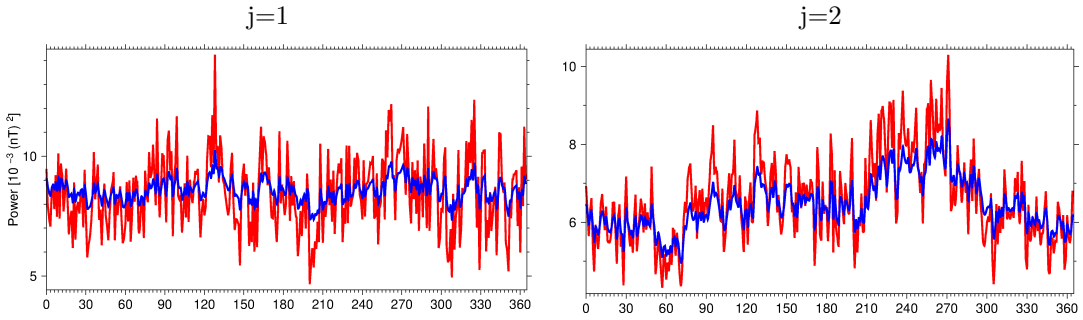

Figure 16: Effect of self-induction on the OIMF power spectrum. Time evolution of the OIMF's power spectra on the lowest degrees computed using the ElmgTD solver with (blue) and without (red) self-induction throughout the year 2007.

E, see Table 2. LSOMG-BT can be used for tidal simulations since it is equiped with the tidal forcing and the parameterizations of SAL and IWD. LSOMG-BT can also be forced by surface wind stress although baroclinic LSOMG is better suited for the wind-driven simulations. We refer to Sec. 4 of the thesis for further details.

The LSOMG model is described in Sec. 5 of the thesis. Here is a brief summary: LSOMG is a C-grid z-coordinate model. The primitive equations in hydrostatic and Boussinesq approximations (see Sec. 1.4) are expressed in orthogonal cuvilinear coordinates using metric coefficients. LSOMG uses the split-explicit time stepping scheme to decrease computational demands and provide fine resolution in time for tidal simulations. The state equation of McDougall et al. [2003] with the values of coefficients from Jackett et al. [2006] is implemented. The friction force for the incompressible fluid, transversely isotropic with respect to the vertical coordinate is used [Murray and Reason, 2001, Einšpigel and Martinec, 2015]. The horizontal friction is discretized explicitly, while the vertical friction is discretized implicitly in time to ensure numerical stability. The horizontal viscosity is the Smagorinsky viscosity [Smagorinsky, 1963, 1993, Griffies and Hallberg, 2000] under CFL, grid-Reynolds and Munk-layer criteria with a

prescribed minimum viscosity. The vertical viscosity is either constant or it is set according to the Richardson-number based parameterization of Pacanowski and Philander [1981]. Three advection schemes with flux limiters are available. All schemes use multidimensional splitting method of Adcroft et al. [2014]. The Coriolis term is treated using spatial-discretization schemes that conserve energy, vorticity or both and using the Adams-Bashforth extrapolation of the third-order in time. The grid-scale noise is suppressed using the divergence-damping method. The dipolar/tripolar grids are implemented to solve the Pole problem. LSOMG is parallelized using the MPI standard. The model is driven by atmospheric forcing and/or tides. Tidal parameterizations are the same as in the LSOMG-BT model. Two barotropic systems are used to separate tidal and non-tidal flows [Sakamoto et al., 2013].

We calculated the flow in the Munk problem, modeled the Ekman spiral in the Ekman layer and tested the advection schemes to check the model performance, see Secs 6.3, 6.4 and 6.5 of the thesis, respectively. In Sec 1.5 of this summary, we presented our numerical tests for ocean tidal models. We recommend not to use the Euler implicit time stepping scheme for tidal simulations. The choice of computational grid matters. B/E-grid configurations suffer from small (several percents) energy leakage due to the biharmonic smoothing of SSH. C-grid configurations do not have these problems. Different boundary conditions on grids B/E and C can have strong impact on the solution especially in the realistic configurations with extensive coastlines.

The LSOMG model results from realistic tidal barotropic simulations, wind-driven barotropic simulations and wind-driven baroclinic simulations were presented in Secs. 1.6, 1.7 and 1.8, respectively.

Fig. 3 demonstrates the importance of IWD and SAL parameterizations for tidal simulations. The RSS computed according to Eq. (20) decreased to approximately one third if IWD and SAL were used (default setup). Fig. 4 shows the sensitivity of RSS on the strength of IWD and SAL. The best setup with IWD increased by factor 1.5 and $\beta_s = 0.11$ has RSS= 10.67 cm which improved the default-setup RSS by 12%.

Figs. 5 and 7 depict LSOMG-BT barotropic stream functions from barotropic simulations forced by the steady wind-driven stress. The simulations with the realistic bathymetry suffer from the virtually missing ACC current; the other currents in the Southern hemisphere are also affected. If bathymetry is flat, the barotropic stream function in the Southern hemisphere improves but the ACC current is overly strong. LSOMG-BT stream functions are stronger if we use the CORE-II instead of ERA-Interim forcing, which matches both SOM simulations and GECCO reanalysis better.

The baroclinic model does not suffer from the ACC problem of the barotropic model. The barotropic stream functions from the baroclinic LSOMG simulations forced by ERA-Interim data are shown in Fig. 11. The stream function is globally stronger (especially in the ACC region) if the full (daily forcing with heat fluxes) rather than simplified (climatological wind stresses, strong surface temperature relaxation) forcing is used. The stronger stream function is in better agreement with other models and data. The increase in the vertical resolution improves the circulation in the Pacific Ocean and it also further strengthens the ACC current. The simulations forced by CORE-II data have better stream function if simple

forcing is used. Both data sets produce comparable circulations if the full forcing is applied. The LSOMG model with the full forcing conserves both temperature and salinity within the range which is comparable with other OGCMs. Figs. 8 and 9 show the SSH and velocities vertically integrated over the upper 1000 m , respectively. The comparison with other models and data products is favourable.

We focused on the modelling of wind-driven OIMF in Sec. 2. In particular, the galvanic coupling is important, see Figs. 13, 14 (top row) and 15 (top row) (epecially Y component). The self-induction effectively damps sudden changes in lower spherical harmonic degrees, see Fig. 16. One layer in the vertical is sufficient for global studies of OIMF, see Figs. 14 (bottom row) and 15 (bottom row), but the local studies should consider a higher vertical resolution. We do not recommend to use unimodal thin sheet approximation of Tyler et al. [1997] and Vivier et al. [2004] since it neglects both galvanic coupling and self-induction. We recommend to use the horizontal resolution of at least 1°.

The paper Velímský et al. [2019] further focuses on the toroidal magnetic field. We used a more realistic spatially variable ocean electrical conductivity and higher vertical resolution. We found the maximum of 15 nT in the Y component of the OIMF in approximately 1800 m depth. At the surface, the toroidal field is zero but it affects the poloidal field through coupling. The observable poloidal field is smaller and its spatial and temporal variability is reduced if there is no couling between the toroidal and poloidal fields.

To sum it up, we have developed a new baroclinic model called LSOMG and studied the OIMF. We answered some questions but there still remain open issues. It is tempting to complete our efforts to detect the wind-driven OIMF in the Swarm data. We should have all necessary components: An OGCM, a magnetic solver and a magnetospheric model. It can however be a tidious work with a possibility that additional pitfalls may apper. A further development of the LSOMG model would also be interesting. We could further improve barotropic tides by locally tuning IWD and SAL. Or study the internal tides in the baroclinic LSOMG altough it would require large computational resources on a supercomputer.

Acknowledgements

This research was supported by the Grant Agency of the Czech Republic, project No. P210/17-03689S, by The Ministry of Education, Youth and Sports from the Large Infrastructures for Research, Experimental Development and Innovations project "IT4Innovations National Supercomputing Center – LM2015070", by the European Space Agency Contract No. 4000109562/14/NL/CBi "Swarm+Oceans" under the STSE Programme, by the Science Foundation Ireland (SFI) grant 11/RFP.1/GEO/3309, and by the Charles University grant SVV 260447.

Bibliography

Y. Accad and C. L. Pekeris. Solution of the tidal equations for the M_2 and S_2 tides in the world oceans from a knowledge of the tidal potential alone. *Phil. Trans. R. Soc. London*, 290(1368):235–266, 1978.

A. Adcroft, J.-M. Campin, S. Dutkiewicz, C. Evangelinos, D. Ferreira, G. Forget, B. Fox-Kemper, P. Heimbach, Ch. Hill, E. Hill, H. Hill, O. Jahn, M. Losch, J. Marshall, G. Maze, D. Menemenlis, and A. Molod. MITgcm user manual. Technical report, MIT Department of EAPS, 2014. URL `http://mitgcm.org/public/r2_manual/latest/`.

C. Amante. ETOPO1 1 arc-minute global relief model: procedures, data sources and analysis. NOAA Technical Memorandum NESDIS NGDC-24, National Geophysical Data Center, NOAA, Boulder, Colorado, 2009. URL `http://www.ngdc.noaa.gov/mgg/global/global.html`.

A. Arakawa and V. R. Lamb. Computational design of the basic dynamical processes of the UCLA general circulation model. *Methods Computat. Phys.*, 17:173–265, 1977.

B. K. Arbic, T. G. Stephen, W. H. Robert, and H. L. Simmons. The accuracy of surface elevations in forward global barotropic and baroclinic tide models. *Deep-Sea Res. II*, 51:3069–3101, 2004.

K. Bryan and L. J. Lewis. A water mass model of the world ocean. *J. Geophys. Res.-Oceans*, 84(C5):2503–2517, 1979.

M. C. Buijsman, B. K. Arbic, J. A. M. Green, R. W. Helber, J. G. Richman, J. F. Shriver, P. G. Timko, and A. Wallcraft. Optimizing internal wave drag in a forward barotropic model with semidiurnal tides. *Ocean Model.*, 85:42–55, 2015.

J. M. Campin, A. Adcroft, C. Hill, and J. Marshall. Conservation of properties in a free-surface model. *Ocean Model.*, 6:221–244, 2004. doi: 10.1016/S1463-5003(03)00009-X.

S. A. Cunningham, S. G. Alderson, B. A. King, and M. A. Brandon. Transport and variability of the Antarctic Circumpolar Current in Drake Passage. *J. Geophys. Res.-Oceans*, 108(C5), 2003.

D. P. Dee, S. M. Uppala, A. J. Simmons, P. Berrisford, P. Poli, S. Kobayashi, U. Andrae, M. a. Balmaseda, G. Balsamo, P. Bauer, et al. The ERA-Interim reanalysis: Configuration and performance of the data assimilation system. *Q. J. Roy. Meteor. Soc.*, 137(656):553–597, 2011. doi: 10.1002/qj.828.

H. Dobslaw, F. Flechtner, I. Bergmann-Wolf, C. Dahle, R. Dill, S. Esselborn, I. Sasgen, and M. Thomas. Simulating high-frequency atmosphere-ocean mass variability for dealiasing of satellite gravity observations: AOD1B RL05. *J. Geophys. Res.*, 118(7):3704–3711, 2013. doi: 10.1002/jgrc.20271. URL `http://doi.wiley.com/10.1002/jgrc.20271`.

D. Einšpigel and Z. Martinec. A new derivation of the shallow water equations in geographical coordinates and their application to the global barotropic ocean model (the DEBOT model). *Ocean Model.*, 92:85–100, 2015. doi: 10.1016/j.ocemod.2015.05.006.

Á. H. Flosadóttir, J. C. Larsen, and J. T. Smith. Motional induction in North Atlantic circulation models. *J. Geophys. Res.: Oceans*, 102(C5):10353–10372, 1997.

E. Friis-Christensen, H. Lühr, and G. Hulot. Swarm: A constellation to study the Earth's magnetic field. *Earth Planets Space*, 58(4):351–358, 2006.

T. Frisius, K. Fraedrich, X. Zhu, and W. Wang. A spectral barotropic model of the wind-driven world ocean. *Ocean Model.*, 30(4):310–322, 2009.

A. J. Gadd. An economical explicit integration scheme. Meteor. office tech. note 44, 1974.

A. V. Grayver, F. D. Munch, A. V. Kuvshinov, A. Khan, T. J. Sabaka, and L. Tøffner-Clausen. Joint inversion of satellite-detected tidal and magnetospheric signals constrains electrical conductivity and water content of the upper mantle and transition zone. *Geophys. Res. Lett.*, 44:6074–6081, 2017.

S. Griffies, A. Gnanadesikan, R. Pacanowski, V. Larichev, J. Dukowicz, and R. Smith. Isoneutral diffusion in a z-coordinate ocean model. *J. Phys. Oceanogr.*, 28:805–830, 1998.

S. M. Griffies and R. W. Hallberg. Biharmonic friction with a Smagorinsky–like viscosity for use in large–scale eddy–permitting ocean models. *Mon. Wea. Rev.*, 128:2935–2946, 2000. doi: 10.1175/1520-0493(2000)128⟨2935:BFWASL⟩2.0.CO;2.

S. M. Griffies, A. Biastoch, C. Böning, F. Bryan, G. Danabasoglu, E. P. Chassignet, M. H. England, R. Gerdes, H. Haak, R. W. Hallberg, et al. Coordinated ocean-ice reference experiments (COREs). *Ocean model.*, 26(1-2):1–46, 2009.

L. Han. A two-time-level split-explicit ocean circulation model (MASNUM) and its validation. *Acta Oceanol. Sin.*, 33(11):11–35, 2014. doi: 10.1007/s13131-014-0553-z.

S. Hellerman and M. Rosenstein. Normal monthly wind stress over the world ocean with error estimates. *J. Phys. Oceanogr.*, 13(7):1093–1104, 1983.

M. C. Hendershott. The effects of solid earth deformation on global ocean tides. *Geophys. J. Int.*, 29(4):389–402, 1972.

S. Imawaki, H. Uchida, H. Ichikawa, M. Fukasawa, S. Umatani, and ASUKA Group. Satellite altimeter monitoring the Kuroshio transport south of Japan. *Geophys. Res. Lett.*, 28(1):17–20, 2001.

IOC, IHO and BODC. Centenary edition of the gebco digital atlas, published on cd-rom on behalf of the intergovernmental oceanographic commission and the international hydrographic organization as part of the general bathymetric chart of the oceans. 2003.

C. Irrgang, J. Saynisch, and M. Thomas. Impact of variable seawater conductivity on motional induction simulated with an ocean general circulation model. *Ocean Sci.*, 12(4):129–136, 2016a. doi: 10.5194/os-12-129-2016.

C. Irrgang, J. Saynisch, and M. Thomas. Ensemble simulations of the magnetic field induced by global ocean circulation: Estimating the uncertainty. *J. Geophys. Res. Oceans*, 121(3):1866–1880, 2016b. doi: 10.1002/2016JC011633.

Ch. Irrgang, J. Saynisch, and M. Thomas. Utilizing oceanic electromagnetic induction to constrain an ocean general circulation model: A data assimilation twin experiment. *J. Adv. Model. Earth Sy.*, 2017. doi: 10.1002/201simu7MS000951.

D. R. Jackett, T. J. McDougall, R. Feistel, D. G. Wright, and S. M. Griffies. Algorithms for density, potential temperature, conservative temperature, and the freezing temperature of seawater. *J. Atmos. Oceanic Technol.*, 23:1709–1728, 2006. doi: 10.1175/JTECH1946.1.

S.R. Jayne and L.C. St. Laurent. Parameterizing tidal dissipation over rough topography. *Geophys. Res. Let.*, 28:811–814, 2001.

G. Kaplan, J. Bartlett, A. Monet, J. Bangert, and W. Puatua. User's guide to NOVAS version F3.1. Technical report, Washington, DC: USNO, 2011. URL `http://aa.usno.navy.mil/software/novas/novas_f/NOVAS_F3.1_Guide.pdf`.

A. B. Kara, P. A. Rochford, and H. E. Hurlburt. Air–sea flux estimates and the 1997–1998 ENSO event. *Bound.-Lay. Meteorol.*, 103(3):439–458, 2002.

A. Kelbert, A. Kuvshinov, J. Velímský, T. Koyama, J. Ribaudo, J. Sun, Z Martinec, and C. J. Weiss. Global 3-d electromagnetic forward modelling: a benchmark study. *Geophys. J. Int.*, 197(2):785–814, 2014.

J. Kondo. Air-sea bulk transfer coefficients in diabatic conditions. *Bound.-Lay. Meteorol.*, 9(1):91–112, 1975.

W. G. Large and S. G. Yeager. Diurnal to decadal global forcing for ocean and sea-ice models: the data sets and flux climatologies. NCAR technical note: Ncar/tn-460+str, CGD Division of the National Center for Atmospheric Research, 2004.

W. G. Large and S. G. Yeager. The global climatology of an interannually varying air–sea flux data set. *Clim. dynam.*, 33(2-3):341–364, 2009.

H. Lei. A two-time-level split-explicit ocean circulation model (MASNUM) and its validation. *Acta Oceanol. Sin.*, 33:11–35, 2014. doi: 10.1007/s13131-014-0553-z.

R. A. Locarnini, A. V. Mishonov, J. I. Antonov, T. P. Boyer, H. E. Garcia, O. K. Baranova, M. M. Zweng, C. R. Paver, J. R. Reagan, D. R. Johnson, M. Hamilton, and D. Seidov. World ocean atlas 2013, volume 1: Temperature. In S. Levitus, editor, *NOAA Atlas NESDIS 73*, page 40. 2013.

G. Madec. NEMO ocean engine (version 3.4). Technical report, Laboratoire d'Océanographie et du Climat: Expérimentation et Approches Numériques, 2012. URL http://www.nemo-ocean.eu/About-NEMO/Reference-manuals.

E. Maier-Reimer and U. Mikolajewicz. The hamburg large scale geostrophic ocean general circulation model (cycle 1). DKRZ report 2, Max–Planck–Institut für Meteorologie, Hamburg, Germany, 1992. URL http://mud.dkrz.de/fileadmin/extern/documents/reports/ReportNo.02.pdf.

C. Manoj, A. Kuvshinov, S. Maus, and H. Lühr. Ocean circulation generated magnetic signals. *Earth Planets Space*, 58(4):429–437, 2006.

N. Maximenko, P. Niiler, L. Centurioni, M.-H. Rio, O. Melnichenko, D. Chambers, V. Zlotnicki, and B. Galperin. Mean dynamic topography of the ocean derived from satellite and drifting buoy data using three different techniques. *J. Atmos. Ocean. Tech.*, 26(9):1910–1919, 2009.

J. L. McClean, D. C. Bader, F. O. Bryan, M. E. Maltrud, J. M. Dennis, A. A. Mirin, P. W. Jones, Y. Y. Kim, D. P. Ivanova, M. Vertenstein, et al. A prototype two-decade fully-coupled fine-resolution CCSM simulation. *Ocean Model.*, 39 (1-2):10–30, 2011.

T. J. McDougall, D. R. Jackett, D. G. Wright, and R. Feistel. Accurate and computationally efficient algorithms for potential temperature and density of seawater. *J. Atmos. Oceanic Technol.*, 20:730–741, 2003. doi: 10.1175/1520-0426(2003)20⟨730:AACEAF⟩2.0.CO;2.

F. Mesinger. Forward-backward scheme, and its use in a limited area model. *Contrib. Atmos. Phys.*, 50:200–210, 1977.

R. J. Murray. Explicit generation of orthogonal grids for ocean models. *J. Comput. Phys.*, 126:251–273, 1996. doi: 10.1006/jcph.1996.0136.

R. J. Murray and C. J. C. Reason. A curvilinear version of the Bryan-Cox-Semtner ocean model and its representation of the Arctic circulation. *J. Comput. Phys.*, 171:1–46, 2001. doi: 10.1006/jcph.2001.6761.

D. Olbers and K. Lettmann. Barotropic and baroclinic processes in the transport variability of the Antarctic Circumpolar Current. *Ocean Dynam.*, 57(6):559–578, 2007.

R. C. Pacanowski and S. G. H. Philander. Parameterization of vertical mixing in numerical models of tropical oceans. *J. Phys. Oceanogr.*, 11(11):1443–1451, 1981.

S. Rahmstorf. A fast and complete convection scheme for ocean models. *Ocean model.*, 101(9.11), 1993.

J. L. Roberts, P. Heil, R. J. Murray, D. S. Holloway, and N. L. Bindoff. Pole relocation for an orthogonal grid: An analytic method. *Ocean model.*, 12: 16–31, 2006. doi: 10.1016/j.ocemod.2005.03.004.

l. Šachl, Z. Martinec, J. Velímský, C. Irrgang, J. Petereit, J. Saynisch, D. Einšpigel, and N. R. Schnepf. Modelling of electromagnetic signatures of global ocean circulation: physical approximations and numerical issues. *Earth Planets Space*, 71(1):58, 2019.

K. Sakamoto, H. Tsujino, H. Nakano, M. Hirabara, and G. Yamanaka. A practical scheme to introduce explicit tidal forcing into an OGCM. *Ocean Sci.*, 9(6):1089, 2013.

J. Saynisch, J. Petereit, C. Irrgang, A. Kuvshinov, and M. Thomas. Impact of climate variability on the tidal oceanic magnetic signal-A model-based sensitivity study. *J. Geophys. Res. Oceans*, 121(8):5931–5941, 2016. doi: 10.1002/2016JC012027.

Friedrich A Schott, Thomas N Lee, and Rainer Zantopp. Variability of structure and transport of the Florida Current in the period range of days to seasonal. *J. Phys. Oceanogr.*, 18(9):1209–1230, 1988.

A. F. Shchepetkin and J. C. McWilliams. The regional oceanic modeling system (ROMS): a split-explicit, free-surface, topography-following-coordinate oceanic model. *Ocean Model.*, 9:347–404, 2005.

A. F. Shchepetkin and J. C. McWilliams. Computational kernel algorithms for fine-scale, multi-process, long-time oceanic simulations. In R. Temam and J. Tribbia, editors, *Handbook of Numerical Analysis: Computational Methods for the Ocean and the Atmosphere*, pages 121–183. Elsevier Science, 2008. ISBN: 978-0-444-51893-4.

J. Smagorinsky. General circulation experiments with the primitive equations: I. the basic experiment. *Mon. Weather Rev.*, 91:99–164, 1963. doi: 10.1175/1520-0493(1963)091⟨0099:GCEWTP⟩2.3.CO;2.

J. Smagorinsky. Some historical remarks on the use of nonlinear viscosities. In B. Galperin and S.A. Orszag, editors, *Large Eddy Simulation of Complex Engineering and Geophysical Flows*, pages 3–36. Cambridge University Press, Cambridge, 1993.

R. Smith, P. Jones, B. Briegleb, F. Bryan, G. Danabasoglu, J. Dennis, J. Dukowicz, C. Eden, B. Fox-Kemper, P. Gent, M. Hecht, S. Jayne, M. Jochum, W. Large, K. Lindsay, M. Maltrud, N. Norton, S. Peacock, M. Vertenstein, and S. Yeager. The Parallel Ocean Program (POP) reference manual ocean component of the Community Climate System Model (CCSM) and Community Earth System Model (CESM). Technical report, Technical Report LAUR-10-01853, Los Alamos National Laboratory, Los Alamos, 2010. URL `http://www.cesm.ucar.edu/models/cesm1.0/pop2/doc/sci/POPRefManual.pdf`.

D. Stammer, R. D. Ray, O. B. Andersen, B. K. Arbic, W. Bosch, L. Carrère, Y. Cheng, D. S. Chinn, B. D. Dushaw, G. D. Egbert, et al. Accuracy assessment of global barotropic ocean tide models. *Rev. Geophys.*, 52(3):243–282, 2014.

D. Stephenson and K. Bryan. Large-scale electric and magnetic fields generated by the oceans. *J. Geophys. Res.: Oceans*, 97(C10):15467–15480, 1992.

M. Thomas, J. Sündermann, and E. Maier-Reimer. Consideration of ocean tides in an OGCM and impacts on subseasonal to decadal polar motion excitation. *Geophys. Res. Lett.*, 28(12):2457–2460, 2001. doi: 10.1029/2000GL012234.

R. Timmermann, S. Danilov, J. Schröter, C. Böning, D. Sidorenko, and K. Rollenhagen. Ocean circulation and sea ice distribution in a finite element global sea ice-ocean model. *Ocean Dyn.*, 27:114–129, 2009. doi: 10.1016/j.ocemod.2008.10.009.

K. E. Trenberth, W. G. Large, and J. G. Olson. The mean annual cycle in global ocean wind stress. *J. Phys. Oceanogr.*, 20:1742–1760, 1990. doi: 10.1175/1520-0485(1990)020⟨1742:TMACIG⟩2.0.CO;2.

R. H. Tyler, L. A. Mysak, and J. M. Oberhuber. Electromagnetic fields generated by a three dimensional global ocean circulation. *J. Geophys. Res.: Oceans*, 102 (C3):5531–5551, 1997.

UNESCO. Background papers and supporting data on the international equation of state of seawater 1980. *UNESCO technical papers in marine sci.*, 36, 1981.

J. Velímský, A. Grayver, A. Kuvshinov, and L. Šachl. On the modelling of M_2 tidal magnetic signatures: Effects of physical approximations and numerical resolution. *Earth Planets Space*, 70(1):70–192, 2018.

J. Velímský, L. Šachl, and Z. Martinec. The global toroidal magnetic field generated in the Earth's oceans. *Earth Planet. Sc. Lett.*, 509:47–54, 2019.

F. Vivier, E. Maier-Reimer, and R. H. Tyler. Simulations of magnetic fields generated by the Antarctic Circumpolar Current at satellite altitude: Can geomagnetic measurements be used to monitor the flow? *Geophys. Res. Lett.*, 31(10), 2004.

A. Voldoire, E. Sanchez-Gomez, D. S. Mélia, B. Decharme, Ch. Cassou, S. Sénési, S. Valcke, I. Beau, A. Alias, M. Chevallier, et al. The CNRM-CM5.1 global climate model: description and basic evaluation. *Clim. Dynam.*, 40(9-10): 2091–2121, 2013.

L. Šachl, D. Einšpigel, and Z. Martinec. Simple numerical tests for ocean tidal models. *Accepted to Stud. Geophys. Geod.*, 2020.

D. L. Williamson, J. B. Drake, J. J. Hack, J. Rüdiger, and P. N. Swarztrauber. A standard test set for numerical approximations to the shallow water equations in spherical geometry. *J. Comput. Phys.*, 102(1):211–224, 1992. doi: 10.1016/S0021-9991(05)80016-6.

C. Wunsch. The decadal mean ocean circulation and Sverdrup balance. *J. Marine Res.*, 69:417–434, 2011.

M. M. Zweng, J. R. Reagan, J. I. Antonov, R. A. Locarnini, A. V. Mishonov, T. P. Boyer, H. E. Garcia, O. K. Baranova, D. R. Johnson, D. Seidov, and M. M. Biddle. World ocean atlas 2013, volume 2: Salinity. In S. Levitus, editor, *NOAA Atlas NESDIS 74*, page 39. 2013.

List of author's publications

Related to the thesis topic

L. Šachl, D. Einšpigel, Z. Martinec. Simple numerical tests for ocean tidal models. *Stud. Geophys. Geod.*, 64:202-240, 2020.

L. Šachl, Z. Martinec, J. Velímský, C. Irrgang, J. Petereit, J. Saynisch, D. Einšpigel, and N. R. Schnepf. Modelling of electromagnetic signatures of global ocean circulation: physical approximations and numerical issues. *Earth Planets Space*, 71(1):58, 2019.

J. Velímský, **L. Šachl**, and Z. Martinec. The global toroidal magnetic field generated in the Earth's oceans. *Earth Planet. Sc. Lett.*, 509:47–54, 2019.

J. Velímský, A. Grayver, A. Kuvshinov, and **L. Šachl**. On the modelling of M_2 tidal magnetic signatures: Effects of physical approximations and numerical resolution. *Earth Planets Space*, 70(1):70–192, 2018.

Non-related to the thesis topic

L. Šachl. Validation of 3-D synthetic seismograms based on the ray-Born approximation. *Stud. Geophys. Geod.*, 57(1): 84-102, 2013.

Z. Martinec, J. Velímský, R. Haagmans, and **L. Šachl**. A two-step along-track spectral analysis for estimating the magnetic signals of magnetospheric ring current from Swarm data. *Geophys. J. Int.*, 212(2):1201–1217, 2017.

S. Sajjadi, Z. Martinec, P. Prendergast, J. Hagedoorn, **L. Šachl**, P. Readman, E. Robin, B. O'Reilly and C. Horan. The unification of gravity data for Ireland-Northern Ireland. *Lead. Edge*, 39(2):135-143, 2020.